Control of Forebody Three-Dimensional Flow Separations

David J. Peake and F. Kevin Owen

May 1979

NASA

National Aeronautics and
Space Administration

CONTROL OF FOREBODY THREE-DIMENSIONAL FLOW SEPARATIONS

David J. Peake
Senior NRC Research Associate
Ames Research Center, NASA
Moffett Field, California 94035, U.S.A.

F. Kevin Owen
Owen International, Inc.
Palo Alto, California 94302, U.S.A.

SUMMARY

Some experiments involving the development of the turbulent symmetric and asymmetric vortex flow about the lee side of a 5° semiangle (θ_c) conical forebody at high relative incidence (α/θ_c) are discussed. The cone was immersed in a Mach 0.6 airstream at a Reynolds number of 13.5×10^6 based on the 1.4-m (54-in.) axial length of the cone.

Novel means of controlling the degree of asymmetry using blowing very close to the nose were investigated. Small amounts of air injected normally or tangentially to the cone surface, but on one side of the leeward meridian and beneath the vortex farthest from the wall, were effective in biasing the asymmetry. With this reorientation of the forebody vortices, the amplitude of the side force could be reduced to the point where its direction was reversed. This phenomenon could be obtained either by changing the blowing rate at constant incidence or by changing incidence at constant blowing rate. Normal injection appeared more effective than tangential injection. The contrarotating vortices in the penetrating jet flow were of opposite hand to the rotational directions of the forebody vortices. A distinctively organized and stable flow structure emerged with the jet vortices positioned above the forebody vortices.

SYMBOLS

Note: All force coefficients are referenced to cone base area = 449.6 cm² (69.7 in.²) and free-stream dynamic pressure.

A	cone base area
C_N, C_{NB}	normal-force coefficient from balance
$C_p = \dfrac{p - p_\infty}{q_\infty}$	local static pressure coefficient
$C_{pp} = \dfrac{p_p - p_\infty}{q_\infty}$	local pitot pressure coefficient
C_Y, C_{YB}	side-force coefficient from balance
C_{Yp}	side-force coefficient from integrated surface pressures at $x/L = 0.87$
$C_\mu = \dfrac{\dot{m} u_j^*}{q_\infty A}$	jet momentum coefficient
D	base diameter of cone = 23.9 cm (9.4 in.)
L	axial length of cone = 137.2 cm (54.0 in.)
$\dot{m}$	jet mass flux
M	Mach number
p	local static pressure
p_p	local pitot pressure
q	dynamic pressure
r	cone radius
R_L	Reynolds number based on axial length of cone and tunnel free-stream conditions
u	local velocity in direction of tunnel axis
u	local velocity, parallel to model axis
u_j^*	sonic jet velocity
v	lateral velocity, normal to tunnel (or model axis)

w	vertical velocity normal to tunnel axis
$\tilde{w}$	vertical velocity normal to model axis
x	distance along tunnel axis
$\tilde{x}$	distance along model axis, origin at pointed apex of cone
y	lateral distance from tunnel (or model axis)
$\bar{y} = \frac{y}{r}$	nondimensional lateral distance
z	vertical distance, normal to tunnel axis
$\tilde{z}$	vertical distance, normal to model axis
$\bar{z} = \frac{z}{r}$	nondimensional vertical distance
ι	angle of incidence
θ_c	cone semiangle
ϕ	circumferential angle around cone surface, measured from windward generator, negative on port side and positive on starboard side (pilot's view from base of cone)

Subscripts

∞	free-stream mean flow conditions
s1	primary separation line
s2	secondary separation line

1. INTRODUCTION

1.1 Flow Asymmetry in the lee- .de Vortex Flow Field at High Angles of Incidence

A present-day missile or military fighter aircraft must perform and be controllable up to high angles of incidence, where complex vortical flow fields exist about the leeward side of the vehicle. These vortices are generated at relatively sharp leading-edge extensions, wing leading-edges, and on the forebody. Once a given ratio of incidence α to seminose angle θ_c (the relative incidence) is exceeded, usually between 1 and 2 for a slender conical or tangent-ogive nose shape attached to a fuselage or cylindrical body, the orientation of the forebody vortices becomes asymmetrical with respect to the meridional plane (Refs. 1-5). (For the cone or tangent-ogive alone, the relative incidence at which the onset of asymmetry occurs is closer to 3.) Substantial side forces and yawing moments then develop to affect the stability of the vehicle. In addition, these forebody vortices, perhaps in conjunction with the vortical flows from the wings, may interfere with downstream control surfaces to provide significant nonlinearities that are unpredictable. Depending on the strengths, locations, and breakdown of these vortices, an aircraft may be departure-prone or departure-resistant to spinning (Ref. 5).

The onset of asymmetry and the initial direction of the side force are responsive to small changes in geometry at the nose, Reynolds number, and Mach number, up to incidences where conditions in the lee-side crossflow become transonic. As speed increases further, the significant side forces disappear (Ref. 2). The asymmetries occur in both laminar and turbulent flows so that transition is presumably not an essential ingredient causing asymmetry. Notwithstanding, the implication from recent tests by Lamont (Ref. 6) with a tangent-ogive cylinder at incidence, at Reynolds numbers encompassing laminar, transitional, and turbulent boundary-layer separation, is that the vortex wake is less structured in the transition domain leading to reduced side and normal forces at a given subsonic Mach number. In the fully laminar or turbulent regions, on the other hand, where the organization of the flow field is well defined, the respective magnitudes of the side force are larger and are closely matched. It is likely that the levels of vorticity and acoustic disturbance in most wind tunnels will also affect the initial occurrence of asymmetries (Ref. 7). A rational explanation for the development of asymmetry in the flow may be related to the stability of the velocity profiles in the vicinity of the saddle singular point that exists in the stream above the body vortices (see Fig. 1). In the example of the flow about a circular cylinder situated perpendicularly to an oncoming stream, Nishioka and Sato (Ref. 8) determined instabilities to amplify initially in the region of the saddle point, to herald the commencement of asymmetric but well-structured wake flow. Thus, for a body of general shape at high incidence, we may conjecture that flow perturbations will impose fluctuations on the saddle point flow that will accentuate the instability mechanism. Evidence points to extremely small surface irregularities in the surface curvature at the nose as governing the initial direction of the asymmetry in the vortex flow field. This is understandable from the fact that a given body at incidence, under identical flow conditions, will provide a repeatable side force direction at a prescribed roll orientation; and near-mirror images of the side-force/incidence performance for roll angles ±90°, as we show in Fig. 2. Despite this knowledge, production tolerances on a typical fighter aircraft may alter the asymmetric vortex flow development sufficiently to provide unpredictable stability problems (Ref. 5). We do not yet understand the influence of geometrical imperfections on the fluid mechanics, nor how the nominally small disturbances of the fluid flow at these imperfections can amplify so considerably. A small flat, for instance, machined in turn on each side of the nose of a fighter/bomber swing-wing aircraft model was effective in completely switching the sign and amplitude of the yawing moment (Ref. 9).

1.2 Control of Asymmetries in the Forebody Vortex Flow Field

As the development of the asymmetry is particularly sensitive to surface curvature or roughness at the nose, it is conceivable that the degree of asymmetry in the forebody flow field could be controlled by deploying a single small strake or by spinning the nose (Ref. 10). The permanent installation of symmetrical nose strakes at the 90° circumferential angle station (Refs. 3, 11) or in helical form from the leeward meridian to the windward meridian (Ref. 12), have been shown to be effective at suppressing the onset of asymmetry, and roughness has been demonstrated to provide a similar benefit (Ref. 3). Unfortunately, the fixing of "add-on" large excrescences to the airframe is usually detrimental to the cruise-drag performance, and strakes that transform the symmetry of the cross section of the nose are accepted less than enthusiastically by radar designers.

It would appear that at forebody relative incidences (incidence to seminose angle, α/θ_c), where asymmetry of the vortex wake commences, we are always dealing not only with separation of the primary boundary layers that develop on each side from the windward generator, but with secondary separations of the lee-side boundary layer in addition (see Fig. 1). The onset of asymmetry would seem to be characterized initially by a rapid, local movement circumferentially of one (or both) secondary separation lines followed, as incidence is increased further, by circumferential movement of the primary separation lines (Refs. 1 and 2). The asymmetric skin friction line pattern on the conical surface development shown on Fig. 3 illustrates this latter flow situation, with "wobbly" primary and secondary separation line traces existing all along the cone (Ref. 13). Here, the free-stream Mach number is 2.94 and the relative incidence is 4.5.

The asymmetric vortex wake usually develops from asymmetric separation line positions on the body, but the latter does not appear to be a necessary condition for the former to occur. An appraisal (Ref. 14) of some earlier, low-subsonic speed tests of Shanks (Ref. 15) where forces and moments were measured on very slender, flat-plate, delta wings (sweep angles from 70° to 84°) at incidence, indicates that even though the separation lines were fixed at the sharp leading-edges, asymmetry in the leading-edge vortices, as determined by the onset of significant rolling moment, occurred when the angle of incidence was about 3 to 4 times the wing seminose angle. This incidence for asymmetry is splendidly illustrated, on the vapor screen pictures (Fig. 4), about another very slender delta wing immersed in a Mach 2.8 flow (Ref. 16). Nonetheless, the sharp edges have a beneficial effect in delaying the onset of asymmetry to higher relative incidences than those obtained with smooth pointed forebodies or forebody/cylinder configurations (Refs. 2-4).

Hence, we have the scenarios of (1) leeward asymmetries in primary and secondary separation line positions coupled with asymmetric vortex flow (Fig. 3, for example), or (2) symmetric fixed primary separation line positions (but asymmetries no doubt, in secondary separation position) in Fig. 4, still yielding asymmetric vortex flow at suitably high angles of attack. The reasons for such flow behavior are evidently complex and perplexing. Nevertheless, the amplification of perturbations to produce an instability at the saddle point (Ref. 3) (and to which we alluded previously) would seem to cover the scenarios presented.

Thus, the objective of the present investigation is to understand the fluid mechanics and to assess the efficacy of making small changes to the nose geometry by novel active or passive means to alter asymmetries in the lee-side flow field about a typical conical forebody. This takes the form of symmetrically and asymmetrically disposed blowing from, respectively, an external compressed air source, or from a combined passive suction/blowing scheme from the windward side to the leeward. Some recent results of Sharir, Portnoy, and Rom (Ref. 17), for instance, have demonstrated the potential for control by symmetrical blowing normal to the surface. They offered the surprising result that blowing symmetrically from jets on the windward side of the nose of a missile configuration provided the most effectiveness in diminishing the side force. We conjecture that blowing from the lee side, in the vicinity of the separation lines, should produce an even greater impression on the asymmetric flow development

It will be noted that in its offering of some comprehension of the fluid mechanics of pneumatically perturbing the asymmetric vortex flow on a typical forebody, this paper is a companion to the paper presented at this meeting by Skow, Moore, and Lorincz (Ref. 18) which discusses the recovery of control and the enhanced stability afforded by nose blowing on a fighter aircraft configuration.

2. MODEL AND EXPERIMENTAL METHOD

A circular cone is the basic nose shape of many flight vehicles. At relative incidences typically less than 3, it provides a useful configuration on which to develop symmetrical three-dimensional separated boundary layers growing, respectively, on the port and starboard sides from the windward meridian to the leeward meridian. Because of the near conicity of the separation lines and vortex development in both subsonic and supersonic turbulent flows (that is, neglecting the effects of transition), the cone also provides a convenient experimental model to explore three-dimensional separations from detailed measurements at only one axial station. In so doing, a quantitative understanding of three-dimensional separation can be obtained that may be applicable to many other complex flow regimes. Above a relative incidence of 3 for the circular cone, however, the lee-side separations become asymmetric in subsonic flow.

Recent measurements have been made of the symmetric and asymmetric flow regimes on a 1.4-m (54-in.) long, 5° semiangle cone, sting-mounted on a roll-gear in the Ames 1.8- by 1.8-m (6- by 6-ft) closed circuit wind tunnel (Fig. 5) at a Mach number of 0.6. Stagnation pressures were subambient, yielding a typical Reynolds number of 13.5×10^5 based on the cone length with nominally zero heat transfer conditions at the cone surface. No artificial tripping of the laminar boundary layer was employed in the nose region. Transition was considered to occur along the initial 20 of the cone length in this wind tunnel at Mach 0.6 where the relatively high acoustic disturbance level equalled 3% of the free-stream dynamic pressure. (Unpublished data by D. Buell and K. Raman, NASA-Ames Research Center.) The cone model was fitted with a slightly blunted tip with a radius of 4% of the base radius.

All detailed measurements on the cone surface ($0° \leq \phi \leq 180°$) and in the lee-side flow field were made at an axial station 0.87 of the cone length aft of the (pointed) apex. Circumferential mean pressure distributions were obtained with 0.51-mm (0.020-in.) diameter static holes spaced at 2-1/2° intervals for $0 \leq \phi \leq 90°$ and at 1° intervals for angles $90° \leq \phi \leq 180°$. These orifices, as well as others along a cone generator and at the 0.85 and 0.95 axial length stations, were connected via "scanivalves" to unbonded

strain-gage pressure transducers. We note that "port" and "starboard" refer to the left-hand and right-hand sides of the cone as a pilot would view them. The positive ϕ direction is on the starboard side.

At a relative incidence of 2.5, where symmetrical separated flow conditions still prevailed, pitot pressures were measured in the lee-side vortex wake with an array of 77 pitot tubes. Supportive three-dimensional laser velocimeter measurements of mean and root-mean-square velocities were obtained at the same relative incidence at the 0.87 axial station. The velocity field in the wake at points in the crossflow plane (perpendicular to the model axis) was measured with a two-color, forward-scatter, frequency-offset laser velocimeter, allowing two velocity components to be obtained simultaneously. A line diagram of the layout of the velocimeter is shown on Fig. 6(a) and a photograph of the sending optics in Fig. 6(b). With this system, the two primary laser lines, namely 4880 and 5145 Å, were separated by means of a prism, P. These primary beams were each split by the Bragg cells B_1 and B_2 to obtain two pairs of divergent, frequency-offset beams. Each pair of beams then passed through a "cube" (C_1 and C_2) that was ground to be slightly "off-square" to rectify the divergence. The four resultant parallel beams proceeded through the sending optics and were focused at the same point within the flow test region. Collecting optics on the far side of the wind-tunnel test section re-focused the scattered light onto a pair of photomultiplier tubes. The signals from those tubes were then processed to obtain two components of velocity of particles passing through the focal volume. Since we were seeking three velocity components, two sets of measurements were taken. In the first set, the laser beams were set normal to the tunnel axis so that the axial (u) and vertical (w) velocity components were found. From these two components the axial and vertical velocities in the crossflow plane perpendicular to the body axis could be resolved (see Fig. 6(c)). For the second set, the transmitting optics were rotated 21° about the z-axis and the measurements repeated. Now, one velocity component measured was again the vertical velocity whereas the second was a combination of the axial velocity (u) and the lateral velocity (v) in wind-tunnel coordinates. Thus, since the axial velocity had already been measured, the lateral velocity could then be calculated. In other words, the lateral velocity in the crossflow plane is obtained, since it is the same in both wind-tunnel and body coordinates.

The Bragg cells, which produce zero-velocity frequency offsets in both color systems, were incorporated to remove directional ambiguity from the measurements. Without this capability, Owen and Johnson (Ref. 19) have cautioned against believing any measurements in flows that are unsteady or possess a high degree of turbulence.

Prior to obtaining the pitot and laser velocimeter measurements at the relative incidence of 2.5, the position of the lee-side vortices adjacent to the cone surface was established under symmetrical and asymmetrical wake conditions utilizing a vapor-screen technique. Water was introduced into the tunnel flow and a thin cross section of the flow, about 2 mm (0.1 in.) thick was illuminated. This was accomplished by passing either the green beam or the blue beam of the laser through a cylindrical lens (Fig. 7). By changing the location of the beam focus, a light sheet of variable divergence angle could be produced to illuminate the crossflow. The lens could be rotated manually about the y-axis and longitudinally and vertically using the velocimeter traverse gear such that any cross-sectional plane in the flow within the field of view circumscribed by the tunnel window could be observed (see Figs. 5 and 7). Photographs of the scattered light were taken with a camera mounted on the sting/strut support, the camera axis being set nominally parallel with the cone surface. Prior to each test run a grid, placed at the axial test station, was photographed; the dimensions of the separated shear layers could then be compared against the grid. This flow visualization experiment was clearly important to determine a suitable mesh area over which to scan the focused laser beams to obtain the flow velocities.

Once the symmetrical separated flow field had been investigated, small amounts of blowing near the nose were introduced in an attempt to control the gross asymmetries in the lee-side flow that develop above a relative incidence of 3. The frustum at the front of the cone model is detachable, as shown in Fig. 8(a). Several new frustra of identical external shape were machined to include blowing holes at various circumferential stations (0°, ±60°, ±120°, and ±150°) and two orifice diameters, 2.4 mm (0.096 in.) and 3.6 mm (0.140 in.) (Fig. 8(b)). The holes were drilled normal to the cone surface at the 12% axial station (from a pointed apex). As well as providing for blowing normal to the surface, sets of right-angle tubes were constructed that could be inserted and glued into one or more of the surface holes to direct the air upstream or downstream along the local cone generator. The air passed to the plenum chamber in the nose frustum via a steel and flexible pipe within the cone model that was supplied with compressed air from an external source. A sensitive throttle valve outside the tunnel permitted control of the blowing pressure up to a maximum of 8 atm in the blowing plenum, corresponding with a maximum rate flow $\dot{m}$ of about 0.023 kg mass/sec (0.0016 slugs/sec). The jet momentum flux was calculated assuming sonic conditions at the jet orifice and a discharge coefficient of 0.8. The thrust coefficient, C_μ, was referenced to the base area of the cone. Note that if the cone length is considered representative of an airplane nose as far back as the cockpit and the airplane is akin to a F-5 fighter, say, an equivalent thrust coefficient based on wing area is 0.05 times C_μ.

Overall force and moment measurements were obtained with an internal strain-gage balance. Mean and root-mean-square forces were measured. (Prior to the test runs, the natural resonances in the cone/sting strut support system were determined by shaking the model in the normal-force and side-force directions.) Initially all blowing ports were blocked with epoxy sealer. Once the no-blowing side-force direction versus incidence performance was ascertained, the appropriate side on which to eject the blowing air was conjectured as that opposite to the direction of the side force. In other words, if the pilot's view were side force to starboard, the starboard vortex would be closer to the surface, and opening a blowing port beneath the port-side vortex would reduce the asymmetry from the jet sink and entrainment effect (see Ref. 18). In a practical aircraft installation, yaw rate as measured on a yaw accelerometer would indicate the appropriate side from which to inject air (or other suitable gas). The degree to which this philosophy was successful and the rationalization for the choice of the circumferential blowing location(s) are presented in the following sections. Typical results are also shown in the form of the effect of incidence on side force development at a constant blowing rate; and the effect of blowing rate on side force at a constant incidence. The effectiveness of symmetrical blowing versus asymmetric blowing is also discussed.

3. RESULTS

3.1 Symmetric Separation of the Lee-Side Cone Flow

The physical characteristics of the symmetric mean flow field about the 5° semiangle cone immersed in a Mach 0.6 stream at a relative incidence of 2.5 were discussed in Ref. 20. Salient features of those results, however, are included to support the present laser velocimeter measurements. Figure 9 displays circumferential pressure distributions at the 0.87 length station for a relative incidence of 2.5. We note good agreement between the two scans of data shown on the respective port and starboard sides. However, between the two sides there is a discrepancy in pressure level which may be attributable to a slightly yawed condition of the model relative to the oncoming free stream.

As the three-dimensional boundary layer develops from the windward attachment line region ($\phi = 0°$) toward the minimum pressure point at $\phi \sim 100°$, the crossflow grows rapidly. Figure 10 is a representative sketch of a typical skin friction line trajectory corresponding with this accelerating flow field. Once past the flank, the boundary layer proceeds around the lee side of the cone and encounters a stiffening adverse pressure gradient (Fig. 9). It thickens rapidly as we see in the laser vapor screen flow visualization photograph on Fig. 11. The angle between the skin friction line and a cone generator gradually reduces to zero (Fig. 10) at which point the skin friction line runs parallel to a generator, the primary separation line, $\phi_{s1} \doteq 145°$. The boundary layer detaches from the surface to form a tightly coiled vortex shown in Fig. 11. Contours of constant pitot pressure deficit in the vortical flow field are plotted in Fig. 12. The vortex core location is close to $\phi = 170°$ above the surface, further evidence of which is shown on the pressure distribution of Fig. 9. At this same circumferential angle, we detect a substantial suction peak on either side of the leeward meridian. This roll-up of the primary boundary layer scavenges fluid from the region of the leeward meridian encouraging a new boundary-layer growth outward and beneath the primary vortex structure. This new boundary layer, after initially accelerating, then meets its own adverse pressure gradient and separates at $\phi_{s2} = 160°$ as a small secondary vortex tucked beneath the primary. The secondary vortex is within the small lobular region shown on the pitot contours of Fig. 12.

The rotational sense of the secondary flow (see Fig. 1) could also be seen when viewing the laser vapor screen through the tunnel window, but is not resolvable from the photographs of the flow. The typical converging skin friction line directions close to the primary and secondary separation lines are drawn on Fig. 10. At the locations of the separation lines, the root-mean-square voltages (normalized by the voltage of the onset mean flow) measured by a buried wire in the cone surface as the cone was rolled about its pitch axis indicated substantial amplification of fluctuation levels. (This can be done, as there is virtually no sensitivity of the symmetrical separated flow to roll orientation, in distinct contrast to the asymmetric flow.) Correspondingly, when the root-mean-square pressure fluctuation at the surface was normalized with respect to the value of the local resultant shear stress, large increases in signal level were also obtained at the separation line positions. These and additional details are explained fully in Ref. 20.

Preliminary assessments of the distributions of axial and vertical velocities in the crossflow plane obtained by the laser velocimeter and shown on Figs. 13 and 14 appear to confirm the dispositions of the primary and secondary vortices in relation to the pitot and vapor screen results. Figure 13, for example, at $\bar{z} = 0.3$, shows that the axial velocity grows from a minimum value at the inboard extremity of the primary vortex (nearest to the meridian plane) to a maximum at the outboard extremity. Maximum values of root-mean-square velocity fluctuations occurred in the vicinity of the core positions (see also Ref. 20). The vertical velocities are shown on Fig. 14. The plot on Fig. 15, obtained from Fig. 14, illustrates the vertical velocity in the meridian plane and indicates the position of the saddle singular point that we drew on Fig. 1. Comparing this result at $\bar{z} = 0.43$ with the region of measured pitot contours shown on Fig. 12, we observe this saddle-point location to be above the extremity of the vortex, in accordance with the flow model postulated on Fig. 1. We note further that in the conjectured crossflow projection (not a conical projection) of the streamlines about the cone cross section in Fig. 1, that the sum of the number of half-saddle singular points at the surface, nodes (foci) and saddle point in the stream, satisfy the appropriate topology law (see Refs. 21 and 22). Hence, this flow topology, verified in most respects by the measurements, appears to be a rational model of the flow.

The lateral velocities, to be obtained from the inclined optics measurements, have not yet been reduced from the data. Sample checks, however, indicate peak values to exist above and below the vortex centers, in accordance with intuitive reasoning.

3.2 Asymmetric Separation of the Lee-Side Cone Flow

Figure 16 is a laser vapor-screen crossflow picture of the Mach 0.6 lee-side separated flow about the cone at a relative incidence of 2.9, once asymmetry has commenced. As incidence is raised further, the secondary vortices (see Fig. 1) become agitated, increasing in unsteadiness to the point of imposing motion on the primary vortices and their associated feeding shear layers. At this particular combination of Mach number, Reynolds number, and cone configuration with 4° nose bluntness, the starboard vortex moved away from the cone surface, tending to roll over on top of the port-side vortex. This event is shown on Fig. 17 as an oblique pilot's view from the port side. The vortices appear more diffuse than in the symmetrical separated flow, but there is no evidence of shedding.

Along with this movement in the lee-side flow structure, we would expect the resultant force vector to move toward the side of the cone against which one vortex is closest (the port side in this case). Figure 18 demonstrates that the initial direction of side force is indeed toward the port side (i.e., a negative side-force coefficient, C_{YB}) in the free-stream Mach number range $0.6 \leq M_\infty \leq 0.95$ at $R_L = 13.5 \cdot 10^6$. A switch in side-force direction will occur if the vortices reverse their disposition so that the starboard vortex is now closest to the surface. Figure 18 illustrates that at Mach 0.6 the reversal is imminent at a relative incidence of about 4.4. At all Mach numbers, we should point out that a small positive offset in C_{YB} exists at low incidences systematic with the discrepancy between the port and starboard pressure distributions displayed on Fig. 9.

As Mach number increases to supersonic, the commencement in divergence of the side force is less precise and is delayed to higher relative incidences. For purposes of comparison, Fig. 19 presents side force versus incidence data taken with the same cone body as used herein but fitted with a sharp apex, in the NAE Ottawa 1.5- by 1.5-m (5- by 5-ft) blowdown wind tunnel at elevated Reynolds numbers, $R_L \sim 35 \times 10^6$. In subsonic flow, the onset of asymmetry occurs at a lower relative incidence with the sharp tip than with the blunt tip. The substantial attenuation of side-force amplitude with increase of Mach number, hinted at in Fig. 18, is demonstrated impressively on Fig. 19. At Mach 4.27, there is no side-force development up to relative incidences of at least 5, under which conditions Rainbird (Ref. 23) has demonstrated the existence of strong embedded shock waves in the lee-side crossflow. These shocks certainly appear to encourage a return to flow symmetry close to the body as we may infer from the highest incidence case shown for the delta-wing flow on Fig. 4.

There is evidently a dependency of onset of asymmetry on cone tip condition (and shape) as well as Reynolds number and Mach number, as we present in summary form on Fig. 20. The critical angle of incidence for the onset of side force is here expressed as the incidence where the side force reaches 5% of the normal force. We note that the onset angle of incidence varies between 2.5 and 4.5 times the cone seminose angle, a range somewhat higher than the nominal value of 2 reported for sharp cones and tangent-ogives by Keener and Chapman (Ref. 3) for Mach numbers less than 0.6. Their onset condition, however, was taken as the incidence where the divergence in side force commenced, and so will always be less than the criterion used above.

3.3 Control by Blowing of the Asymmetry in the Lee-Side Cone Flow

3.3.1 Side Force/Incidence Performance with a Constant Rate of Normal or Tangential Blowing

We speculated in section 2 (and see Ref. 18) that the injection of a small quantity of air from one side beneath the vortex farthest from the surface would tend to reduce the asymmetry in the lee-side vortex pair, the turning and penetrating jet flow providing an entrainment effect on the vortex. In section 3.2, we learned that the secondary vortices became violently unsteady once asymmetry began and incidence continued to increase. Consequently, the first blowing position tried was a single orifice at $\phi = 150°$ and was situated nominally between the locations of the primary and secondary separation lines (see Fig. 10). Before opening a blowing hole, however, the development of the side force with incidence was measured; the test was then repeated with the epoxy sealer removed from the blowing hole, but with no air injection, to determine whether the roughness of the hole itself had an influence. The usual result was that hole roughness introduced on the lee-side of the cone made negligible change to the relative incidence at which significant side force developed.

The effect of blowing normally to the cone surface from a single 2.4-mm (0.096-in.) diameter hole at $\phi = 150°$ is shown as Configuration 3 in Fig. 21. In contrast with the original cone nose labeled Configuration 1, whose initial side-force tendency was illustrated in Fig. 18 to be to port (negative C_{YB}) this replacement nose (Configuration 2) developed side force to the starboard side. Hence the blowing hole was opened at $\phi = -150°$ beneath the high vortex situated on the port side. The introduction of the jet air with $C_\mu \sim 0.003$ at relative incidences up to 2.5 exacerbated the no-blow C_{YB} magnitudes by many times C_μ. Once a relative incidence of 3 was reached, however, the jet became highly interactive with the lee-side vortices to cause a complete reversal in the trend of side-force development. In Fig. 21, we see that the side-force coefficient reduces rapidly to zero and increases in the opposite direction to that of the no-blowing case. Figure 21 also displays that the root-mean-square amplitude of the side-force fluctuation (obtained from the balance) is attenuated at high incidence once the blowing is activated.

If the one blowing orifice between the primary and secondary separations can exercise such powerful control by fluid amplification, what would be the effect of two jets? A second orifice of the same size of 2.4 mm (0.096 in.) was then opened at $\phi = -120°$. This orifice was situated on the windward side of the primary separation line and is denoted as Configuration 4. In Fig. 21, we demonstrate no additional improvement with two holes blowing over the performance with the single orifice. The significant controlling influence is exerted, evidently, inboard of the primary separation line. Hence the windward position of blowing chosen as optimum by Sharir, Portnoy, and Pom (Ref. 17) on a missile configuration would not necessarily seem to be the most applicable.

A test with a larger blowing orifice was then attempted. Another conical nose frustum was attached to the cone body in which 3.6-mm (0.140-in.) diameter blowing orifices had been machined, Configuration 5. Figure 22 shows that the no-blowing side-force/incidence characteristic for Configuration 5 is once again different than the two previous no-blowing cases (Configurations 1 and 2). The initial direction of the side force is toward the port side but reverses at a relative incidence of 3.6. To control the initial direction of side-force, a blowing orifice was opened at $\phi = 150°$ on the starboard side, Configuration 6. Figure 22 shows that blowing at $C_\mu = 0.006$ provided a positive reversal in the initial trend of side-force development, which with increasing incidence, continued to generate ever-increasing positive C_{YB}.

Figure 22 also demonstrates the acceptable repeatability obtainable for the given nose over a spread of days between tests.

Next, a passive suction/blowing scheme was tried by opening another 3.6-mm (0.140 in.) diameter hole at $\phi = 0°$ on the windward ray. This is called Configuration 7. With the external supply of compressed air closed off, air from the approaching windward flow could enter the plenum within the frustum and exhaust out of the $\phi = 150°$ hole on the leeward side. The inflow through the $\phi = 0°$ hole was smoothed by means of a countersunk "bell-mouth" entry. Figure 22 shows that no alleviation in side-force divergence occurred when comparing the results with the no-blowing case. A partial explanation for the failure may be attributed to a significant flow loss in the windward hole leaving only a marginal pressure difference to drive any "injected" air through the second orifice on the leeward side.

Does a symmetrical blowing geometry offer an improvement over the asymmetric schemes looked at so far? Retaining the two open orifices at $\phi = 0°$, $150°$ as in Configuration 7, the $\phi = -150°$ orifice on the port side was also unplugged (Configuration 8), allowing air to issue symmetrically about the cone. The side-force/incidence performance for this latter blowing arrangement is also displayed in Fig. 22. We detect that

the symmetrical blowing rate of $C_\mu \sim 0.010$ del $_{J}$s the onset of asymmetry up to a relative incidence of at least 3.4, but loses its effectiveness at higher incidences. In terms of degree of side-force control per unit blowing mass or momentum flux, we might infer, from comparing Figs. 21 and 22, that the asymmetric single hole blowing scheme at $\phi = 150°$ is the most effective.

The windward hole at $\phi = 0°$ was plugged. The result of inserting one right-angle tube in the 3.6 mm (0.140-in.) diameter hole at $\phi = 150°$ with the blowing exit directed along a body generator towards upstream, is shown in Fig. 23. We see that the initial divergence in side force without blowing (Configuration 9) is erased when the injected air issues at $C_\mu \sim 0.005$ (Configuration 10). Blowing in the downstream direction provides a similar, favorable result (Configuration 12 and see Ref. 18).

It is remarkable, perhaps, that the _direction_ of blowing, whether normal, or tangential upstream or tangential downstream, makes negligibly small difference to the degree of control available (compare Figs. 22 and 23). It is as though the asymmetric jet, in terms of its effect on the forebody flow, may be thought of as a "controllable roughness element." Notwithstanding, the role of the jet in the development of the lee-side flow field is evidently more complex and striking than this analogy might allow, as we see on the sequence of laser vapor screen pictures demonstrated in the next section.

3.3.2 Cone Surface Pressures and Laser Vapor Screen Flow Visualization during an Incidence Sweep with a Constant Rate of Normal Blowing, Configuration 6

In Fig. 24, we view selected laser vapor screen pictures and circumferential distributions of surface pressure at the 0.87 axial station for Configuration 6 with a constant blowing rate, $C_\mu \sim 0.006$. These results correspond with the side-force/incidence performance illustrated in Fig. 22, at relative incidences of 0.43, 1.26, 2.08, 2.48, 2.9, and 3.72. The flow visualization pictures are views from the pilot's position, behind the cone base. The bright appearance of the jet/vortex flow, in contrast with the shadowy nature of the vortices with no jet flow shown on Figs. 11 and 16, is thought to be associated with intense scattering of laser light from additional condensation occurring in the jet-vortex flow due to a low stagnation temperature in the jet air.

At low incidences, Figs. 24(a) and (b) illustrate that the under-expanded jet penetrates into the stream from the $\phi = 150°$ orifice, turning rapidly as it plumes outwards. The contra-rotating vortices of the jet flow itself are of opposite sign to those on the cone (with eventual separation) and are contained within the mushroom-shaped top of the vapor cloud. The pressure distributions on the same figures indicate no clearly determinable perturbations resulting from the jet flow. At relative incidences of 2 and above on Figs. 24(c)-(f), the flow visualization shows the jet as a separate snake-like entity existing above the body vortices. The flow visualization records at relative incidences of 2.08 and 2.48, and the pressures in Figs. 24(c) and (d), both correspond with overall side-force magnitudes near zero. Further increase in relative incidence in Figs. 24(e) and (f) shows a striking difference between the size of the port and starboard vortices, with the starboard vortex, as it is closer to the surface, providing noticeable peaks in suction pressure and hence side force to the right. The mushroom cap to the vapor cloud becomes kidney-shaped concomitant with a counterclockwise rotation of the jet vortices as we see in the hypothesized flow structures in Fig. 25. We note that at the highest relative incidence of 3.7 shown in Fig. 24(f), the jet flow has appeared to ally itself with the (weaker) port-side vortex. The equivalent pressure distribution in Fig. 24(f) displays a complete asymmetry at all circumferential locations.

The essential difference between the alternative flow structures shown on Fig. 25 is the saddle-point formation above the body vortices. If any magnification of instabilities in the region of the enclosing saddle point (see Fig. 1) is the governing flow mechanism promoting vortex asymmetry (roughness and waviness at the nose simply providing the initial direction that the side force should take) then Fig. 25(a) allows that the movement of the saddle point of Fig. 1 to a location well away from the body, above the forebody vortices plus jet, should reduce the influence of the saddle point. The sketch in Fig. 25(b), on the other hand, still permits the enclosing saddle point on Fig. 1 to be positioned close to the body surface where its influence on the adjacent flow field would still be dominant. Summing up this conjectural discussion, we might imply that Fig. 25(a) is a more credible flow topology, therefore, than that shown on Fig. 25(b), and can perhaps be better fitted within the vapor screen boundary on Fig. 24(f).

3.3.3 Effect of Changing Blowing Rate on Side-Force Magnitude at Constant Incidence

Figure 26 presents the control of the asymmetric side forces exercised by changing the blowing rate for those configurations (2, 4, 6, and 8) that utilize normal jets. In all cases, a relative incidence of 3 or greater was chosen for the comparison corresponding with the A, B, and C positions on the (no-blowing) side-force/incidence plots of Figs. 21 and 22.

As blowing rate is increased, Configurations 2 and 4 utilizing the 2.4-mm (0.096-in.) asymmetrically disposed blowing orifices do not demonstrate a capacity to reverse the direction of the side force. The maximum change in amplitude is about a 50% reduction. On the other hand, Configuration 6 with the 3.6-mm (0.140-in.) diameter blowing orifice demonstrates powerful control over side-force development. Depending on blowing rate, C_{YB} can be set at a positive or negative value, with good repeatability. The usefulness of symmetrical normal blowing with Configuration 8 (at $\phi = \pm150°$ and 0°, it will be remembered) is also recognizable. It would appear from Fig. 26 that symmetrical blowing is not as powerful as the asymmetric jet, but can nevertheless keep the side force within acceptable limits.

Figures 27(a)-(g) show laser vapor screen flow visualization results and corresponding circumferential wall static pressure distributions for Configuration 6 at a fixed relative incidence of 3.3 and a varying C_μ. These examples relate to the curve of side force with change of normal blowing rate on Fig. 26 which exhibited the most powerful control and reversal of side-force direction.

The selection of Figs. 27(a)-(c) demonstrates flow features where there is a trickle of blowing air and the stronger port-side vortex generates a negative C_{YB}. The jet flow appears "attached" to the weaker starboard vortex. Figure 27(d) displays the flow field, close to zero side force, where the body vortices are virtually symmetrically displaced and the port and starboard pressure distributions show little disagreement.

Increasing C_μ above 0.004 in Figs. 27(e)-(g) now drives the side force to an ever-increasing positive value, clearly demonstrated by the lengthening distance displayed between the port-side vortex and the cone surface. Note again that the jet flow becomes inseparable from the weaker vortex.

Clearly the symmetry of the body vortices can be controlled by the jet momentum rate, and this symmetry reflects immediately on to the body pressure field. The asymmetry in the jet flow "suspended above" the body vortices appears to be of lesser importance. Because the rotation of the vortices in the jet flow is of opposite hand to the body vortices, the jet flow cannot engulf them, nor can the jet be entrained into them. The speculative jet sink effect introduced earlier is presumably inadmissible. The jet flow will exist as a discrete entity in analogy, perhaps, with the spiral vortices emanating from foci on the nose region of a blunt body (Refs. 21 and 22). The rotational direction of these nose vortices is replicated in the jet flow. We postulate that these spiral vortices on the blunt body have a stabilizing effect on the lee-side flow field to provide a delayed onset of side force. The characteristic mechanism of the jet flow is to give a new structure or topology to the overall flow field (jet vortices plus body vortices) which at a suitable blowing rate offers a not dissimilar flow to that about the blunt body.

Finally, Fig. 28, for the same chosen incidence as in Fig. 27, compares the effectiveness of blowing tangentially upstream or downstream (Configurations 10 and 12, respectively) with that of normal blowing (Configuration 6). All blowing geometries possess the capability to reverse the direction of the side-force development, but the normal blowing has a wider range of applicable C_μ. The effectiveness of the tangential blowing at altering side-force magnitude diminishes at the higher blowing rates. Note, however, that for very small C_μ values typically less than 0.0015, the trend of changing side force with C_μ is of opposite hand to the trend when $C_\mu > 0.0015$.

4. CONCLUSIONS

Based on the pressures, forces, and laser vapor screen measurements about a 5° semiangle cone in a Mach 0.6 flow under turbulent conditions, we may offer the following conclusions on the continuing exploration of the symmetrical separated flow zones at moderate relative incidence ($\alpha/\theta_c \sim 2.5$) and the effectiveness of nose blowing to control asymmetry of the lee-side vortex flow field at high relative incidences ($\alpha/\theta_c \sim 4$):

1. The capability of a new dual-beam laser velocimeter has been exploited to measure the mean velocities in the symmetrically separated flow field and to determine the location of the saddle point above the body vortices in the plane of the leeward meridian. Together with pitot measurements and dimensioning of the boundary of the rolled-up shear layer from the laser flow visualization records, wall pressures, wall shear stresses and directions, plus previously obtained dynamic measurements at the surface (see Ref. 20), a panorama of three-dimensional flow separation is gradually being assembled. The importance of amplification of instabilities at the saddle point, in promoting forebody vortex asymmetry is mooted but has not yet been established; nor whether such amplification by close association with flow near the surface, causes the (eventual massive) unsteadiness of the secondary separations at high relative incidences. Hence, the initial attempt was made to control the asymmetry by injecting air close to one or both of the secondary vortices, and by implication, the region in the vicinity of the saddle point.

2. Blowing on one side of the leeward meridian, from a single circumferential hole situated between the primary and secondary separation lines, but beneath the (weaker) vortex that is farthest from the surface, offers an effective means to reduce to zero (and to subsequently reverse) the direction of the side force.

3. Blowing normal to the surface as a jet spoiler appears to be more effective than either upstream or downstream directed tangential blowing.

4. In contrast to the asymmetric blowing principle, symmetrically disposed blowing nozzles appear less effective at corresponding momentum rates.

5. The blowing rates required are very small, there being a large "fluid amplification" of the jet effect. A typical C_μ required for an aircraft could be as low as 0.001 for an equivalent blowing location.

6. The jet does not engulf the forebody vortices in either the normal or tangential blowing arrangements. Its counter-rotating pair of vortices "float above" the forebody vortices forming a well-organized and recognizable topology. This is so for all blowing geometries, but with the tangential blowing, the structure is less well defined.

REFERENCES

1. Rainbird, W. J., Crabbe, R. S., Peake, D. J., and Mever, R. F., "Some Examples of Separation in Three-Dimensional Flows," CASI Journal, Vol. 12, No. 10, December 1966, pp. 409-423.

2. Peake, D. J., Rainbird, W. J., and Atraghji, E. G., "Three-Dimensional Flow Separations on Aircraft and Missiles," AIAA Journal, Vol. 10, No. 5, May 1972, pp. 567-580.

3. Keener, E. R. and Chapman, G. T., "Onset of Aerodynamic Side Forces at Zero Sideslip on Symmetric Forebodies at High Angles of Attack," AIAA Paper 74-770, August 1974.

4. Keener, E. R., Chapman, G. T., and Kruse, R. L., "Effects of Mach Number and Afterbody Length on Onset of Asymmetric Forces on Bodies at Zero Sideslip and High Angles of Attack," AIAA Paper 76-66, January 1975.

5. Titiriga, A., Skow, A. M., and Moore, W. A., "Forebody/Wing Vortex Interactions and their Influence on Departure and Spin Resistance," AGARD CP-247, October 1978.

6. Lamont, P. J., "Pressure Distributions on an Ogive-Cylinder at High Angles of Attack with Laminar, Transitional or Turbulent Separation," Working Group Meeting on High Angle of Attack Missile Aerodynamics, AEDC, Tennessee, March 1979.

7. Hunt, B. L. and Dexter, P. C., "Pressures on a Slender Body at High Angle of Attack in a Very Low Turbulence Level Airstream," AGARD CP-247, October 1978.

8. Nishioka, M. and Sato, H., "Mechanism of Determination of the Shedding Frequency of Vortices Behind a Cylinder at Low Reynolds Numbers," Journal Fluid Mechanics, Vol. 89, Part 1, 1978, pp. 49-60.

9. Ericsson, L. E. and Reding, J. P., "Coupling Between Boundary-Layer Transition and Vehicle Motion," Working Group Meeting on High Angle of Attack Missile Aerodynamics, NASA Langley Research Center, March 1978.

10. Neihouse, A. I., Klinar, W. J., and Scher, S. H., "Status of Spin Research for Recent Airplane Designs," NASA TR-R-57, 1960.

11. Jorgensen, L. H., "Prediction of Aerodynamic Characteristics for Slender Bodies Alone and with Lifting Surfaces to High Angles of Attack," AGARD CP-247, 1978.

12. Rao, D. M., "Side-Force Alleviation on Slender, Pointed Forebodies at High Angles of Attack," AIAA Paper 78-1339, August 1978.

13. Bannink, W. J. and Nebbeling, C., "Measurements of the Supersonic Flow Field Past a Slender Cone at High Angles of Attack," AGARD CP-247, October 1978.

14. Keener, E. R. and Chapman, G. T., "Similarity in Vortex Asymmetries over Slender Bodies and Wings," AIAA Journal, Vol. 15, No. 9, September 1977, pp. 1370-1372.

15. Shanks, R. E., "Low-Subsonic Measurements of Static and Dynamic Stability Derivatives of Six Flat-Plate Wings Having Leading-Edge Sweep Angles of 70° to 84°," NASA TN D-1822, 1963.

16. Fellows, K. A. and Carter, E. C., "Results and Analysis of Pressure Measurements on Two Isolated Slender Wings and Slender Wing-Body Combinations at Supersonic Speeds, Vol. 1 - Analysis," ARA Rept. 12, November 1969.

17. Sharir, D., Portnoy, H. and Rom, J., "A Study of the Effects of Jets from a Slender Body of Revolution on the Side Forces Acting on It at Large Angles of Attack in Low Speeds," Technion, Israel Institute of Technology, TAE 337, May 1978.

18. Skow, A. M., Moore, W. A., and Lorincz, D. J., "A Novel Concept to Enhance Departure/Spin Recovery Characteristics of Fighter Aircraft Through Control of the Forebody Vortex Orientation," Paper 24, this meeting.

19. Owen, F. K. and Johnson, D. A., "Wake Vortex Measurements of Bodies at High Angle of Attack," AIAA Paper 78-23, January 1978.

20. Peake, D. J., Owen, F. K., and Higuchi, H., "Symmetrical and Asymmetrical Separations about a Yawed Cone," AGARD CP-247, October 1978.

21. Peake, D. J. and Tobak, M., "Three-Dimensional Separated Flows: Retrospect and Prospect," Paper presented at Project Squid Meeting, Dallas, Texas, January 1979.

22. Peake, D. J. and Tobak, M., 'Topology of Two-Dimensional and Three-Dimensional Separated Flows," Paper to be presented at AIAA 12th Fluids and Plasma Dynamics Meeting at Williamsburg, Va., July 1979.

23. Rainbird, W. J., "The External Flow Field About Yawed Circular Cones," AGARD CP-30, May 1968.

ACKNOWLEDGMENTS

Σ_N = NO. OF NODES (FOCI) = 4

Σ_S = NO. OF SADDLES = 1

$\Sigma_{S'}$ = NO. OF HALF SADDLES AT WALL = 8

$\therefore \Sigma_N - (\Sigma_S + \frac{1}{2}\Sigma_{S'}) = -1$

THIS SUMMATION SATISFIES CROSS-FLOW TOPOLOGY LAW (REFS. 21, 22)

ENCLOSING SADDLE POINT

SECONDARY SEPARATION LINE

PRIMARY SEPARATION LINE

Fig. 1. Cross-flow topology of streamlines about circular cone at incidence with primary and secondary separations.
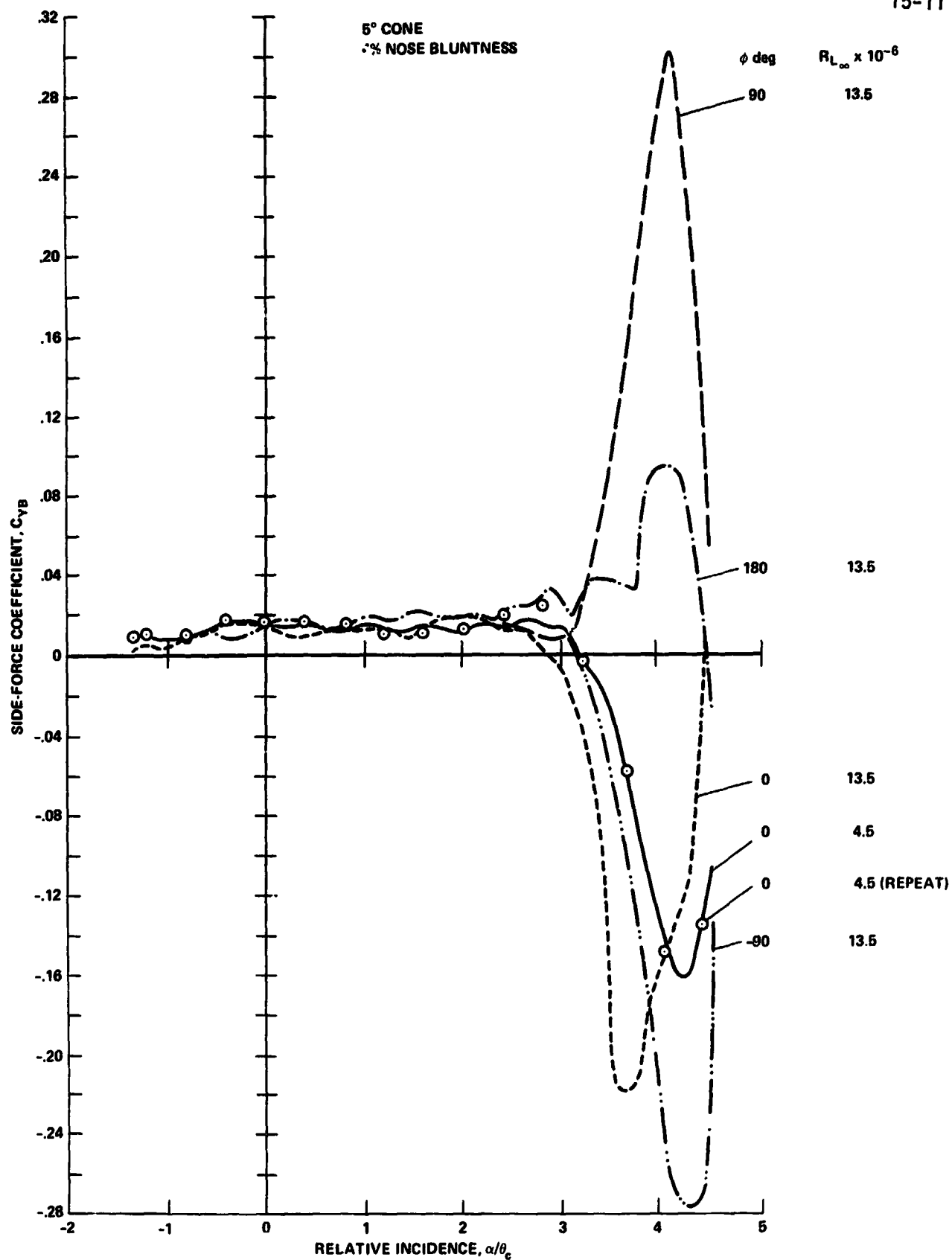
Fig. 2. 5° semiangle cone side-force sensitivity to roll angle and Reynolds number at $M_\infty = 0.6$.
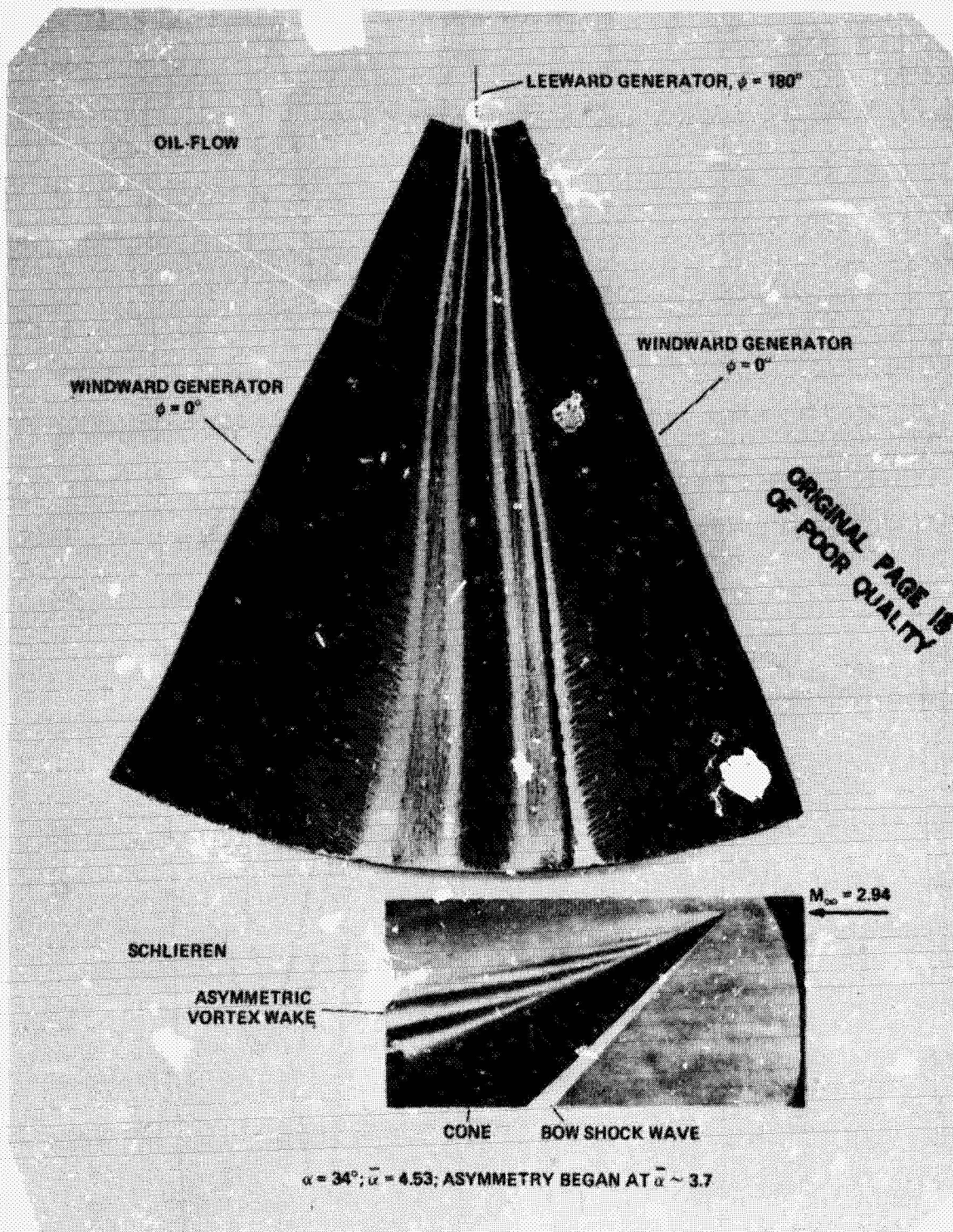
Fig. 3. Asymmetric primary and secondary separation lines on $\theta_c = 7.5°$
semiangle cone (Ref. 13).

α = 19°

α = 18°

α = 17°

α = 15°

α = 10°

α = 36°

α = 28°

α = 22°
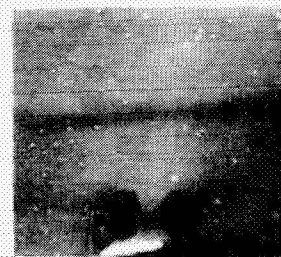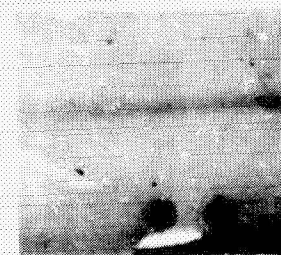
α = 20°

$M_\infty = 2.8$

Fig. 4. Asymmetric flow field about 85° swept back delta wing (Ref. 16).
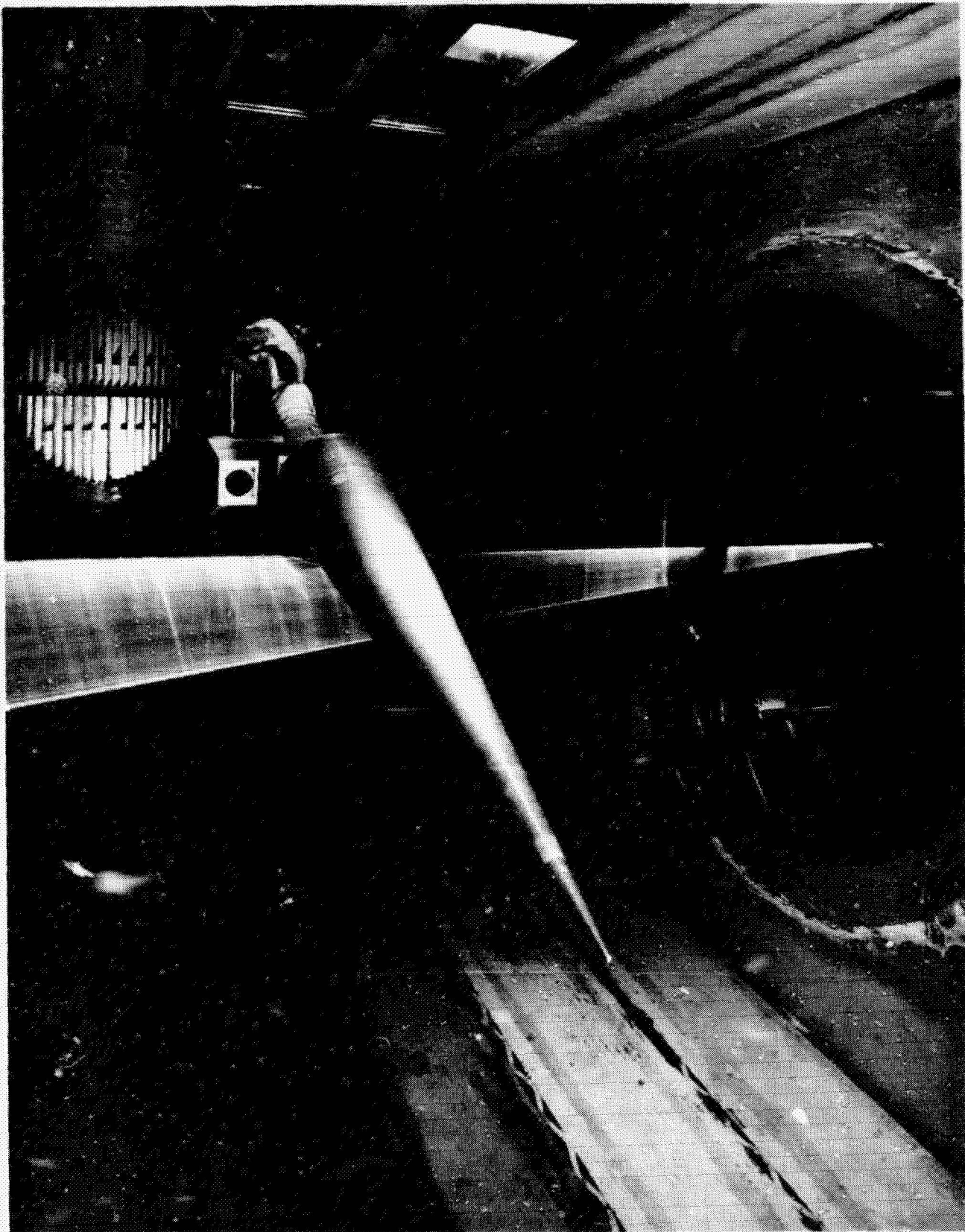
Fig. 5. 5° semiangle cone in Ames 6- by 6-Foot
Wind Tunnel.
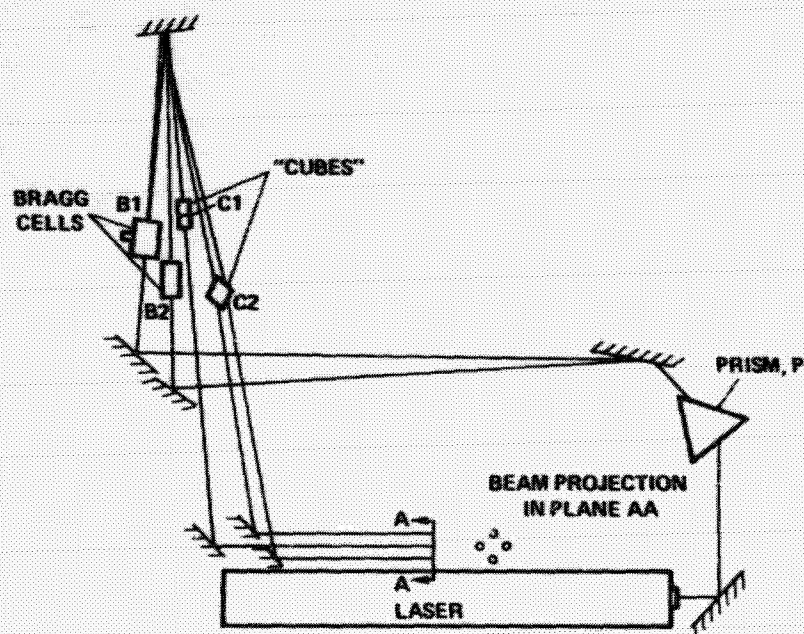
(a) Two-component LDV beam system in Ames
        6- by 6-Foot Wind Tunnel.

Fig. 6.   Velocity measurements with laser velocimeter.
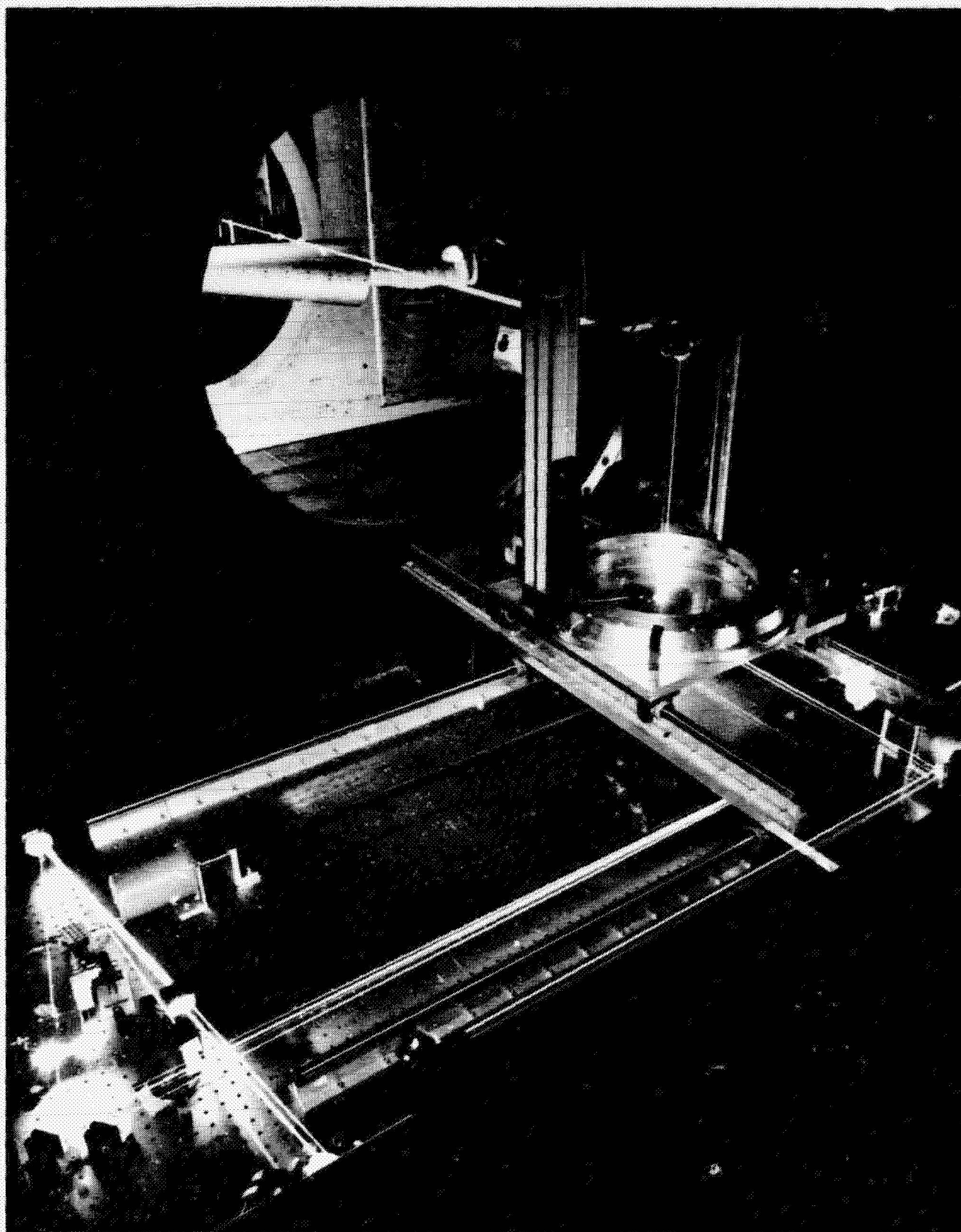
(b) Sending optics and traverse gear of two-component
LDV.

Fig. 6. Continued.
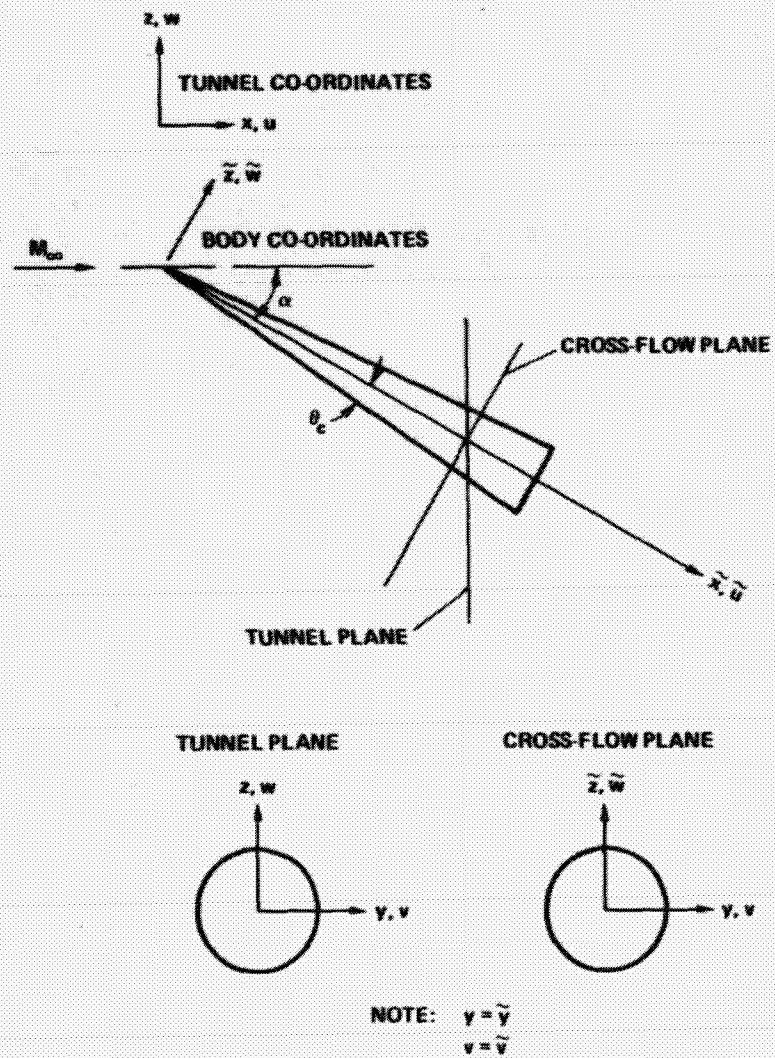
(c) Coordinate system for flow velocities.

Fig. 6. Concluded.
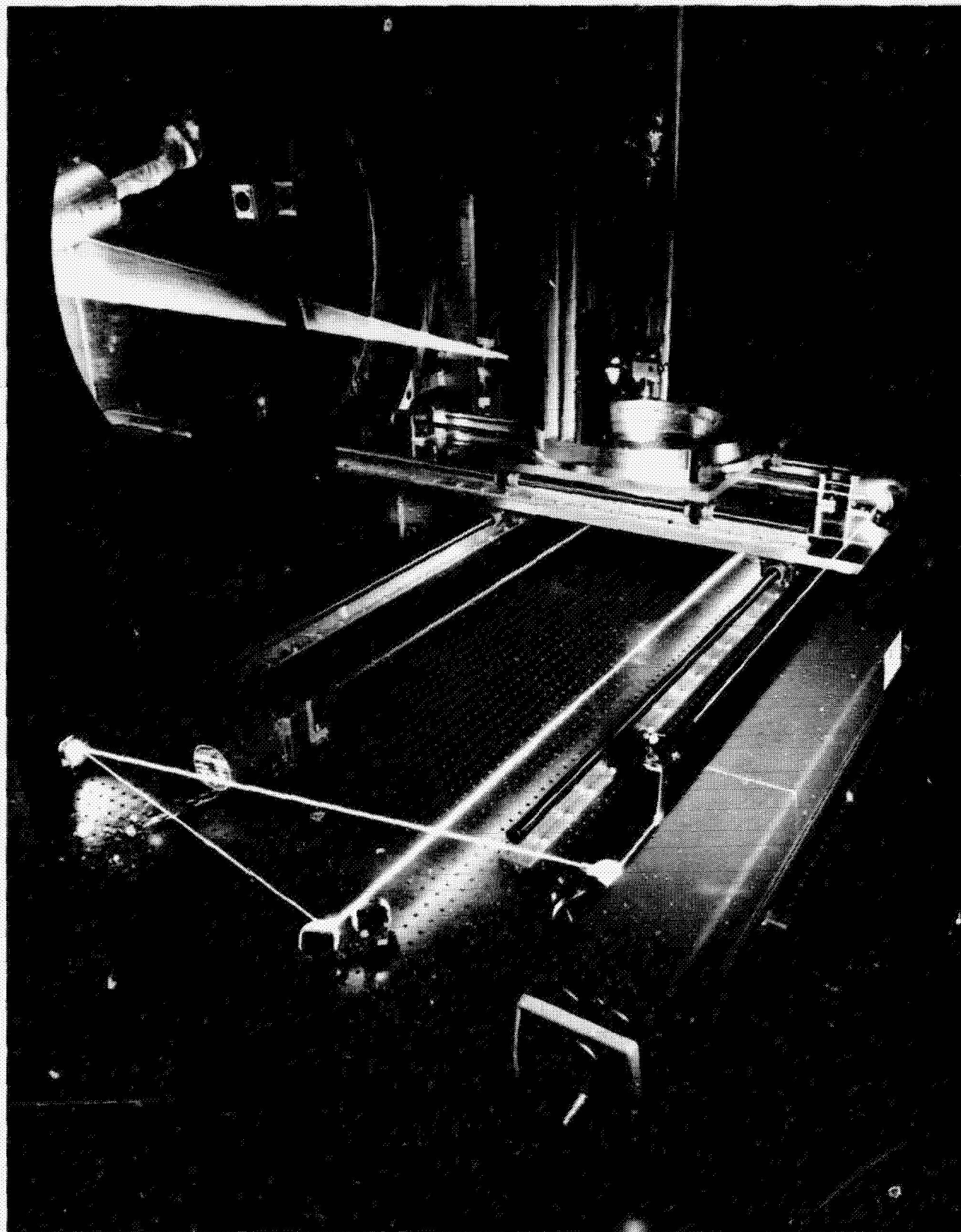
Fig. 7. Spread laser beam for vapor screen.

BLOWING HOLES AT X/L = 0.12
AT φ = 0°, ±60°, ±120°, ±150°
(RIGHT ANGLE TUBES MAY BE
INSERTED INTO ANY HOLE)

HOLLOW FRUSTUM

BLOWING PIPE

$\theta_c = 5°$

COMPRESSED
AIR

NOSE RADIUS = 4% BASE RADIUS = 4.8 mm (0.19 in.)
CONE LENGTH, L = 1.37 m (54 in.)
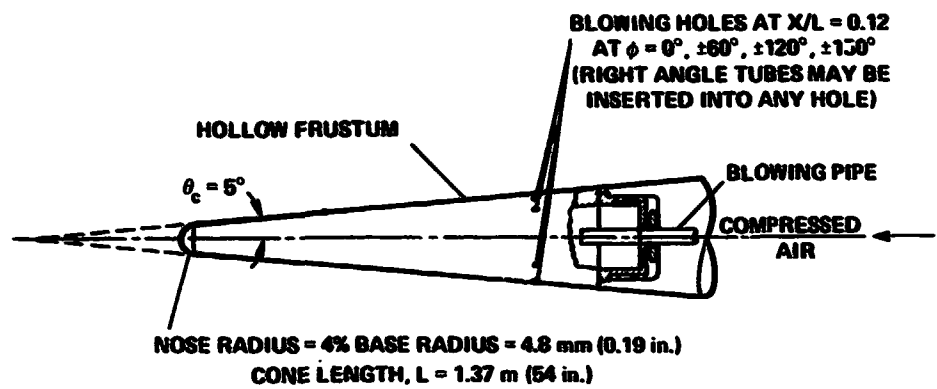
(a) Blowing plenum in conical frustum.

NO.	$\phi°$	JET diam, mm (in.)		NO.	$\phi°$	JET diam, mm (in.)	
1		NONE		7	0, 150	3.6 (0.140)	PASSIVE
2	-150	2.4 (0.096)		8	0, ±150	3.6 (0.140)	
3	-150	2.4 (0.096)		9	150	3.4 (0.132),	TUBE FACING UPSTREAM NO BLOWING
4	-120, -150	2.4 (0.096)		10	150	3.4 (0.132),	TUBE FACING UPSTREAM BLOWING
5	150	3.6 (0.140)		11	150	3.4 (0.132),	TUBE FACING DOWNSTREAM NO BLOWING
6	150	3.6 (0.140)		12	150	3.4 (0.132),	TUBE FACING DOWNSTREAM BLOWING

(b) Normal and tangential jet positions (pilot's view of body cross sections).

Fig. 8. Blowing design.
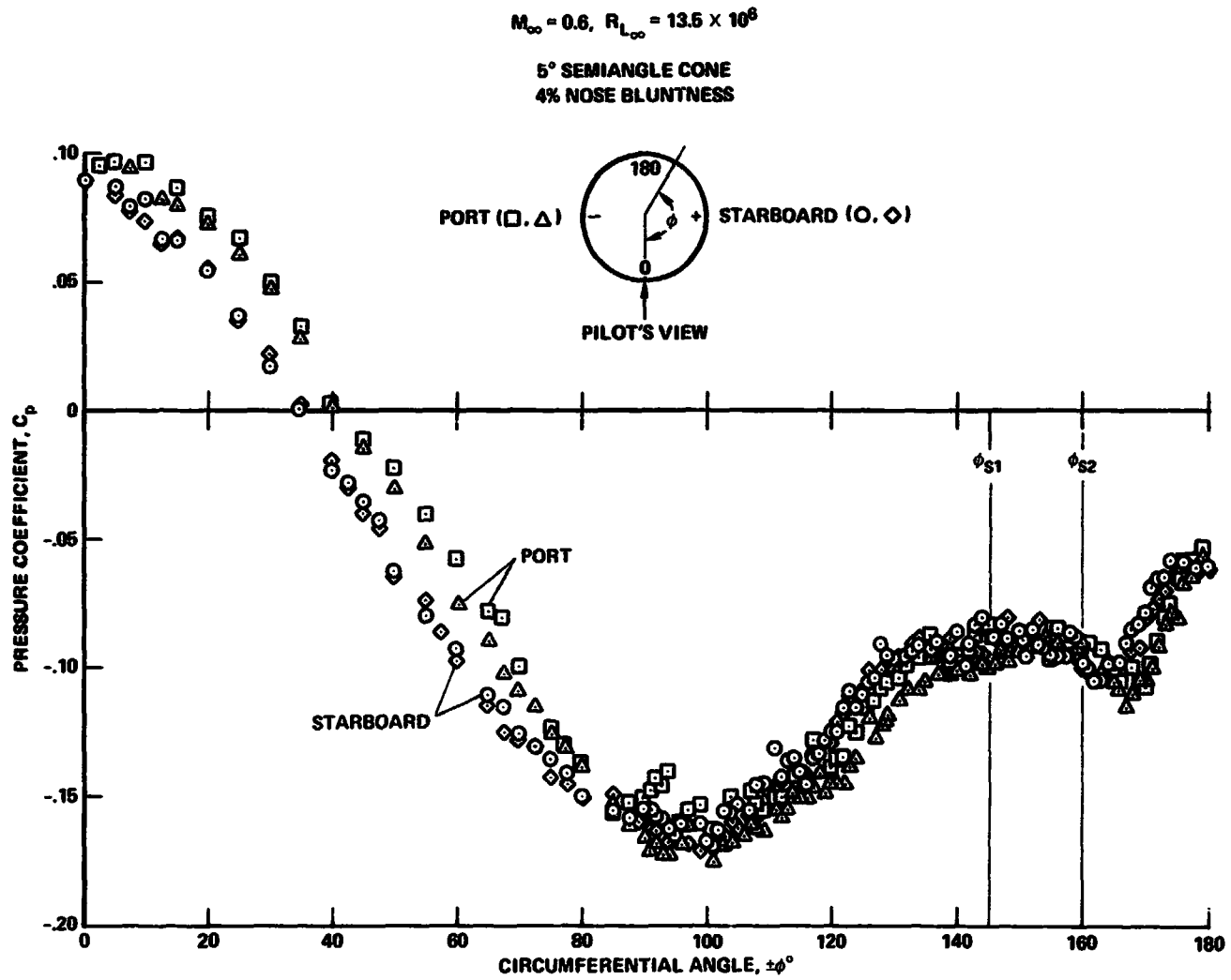
Fig. 9. Surface pressures at $\alpha/\theta_c = 2.5$.
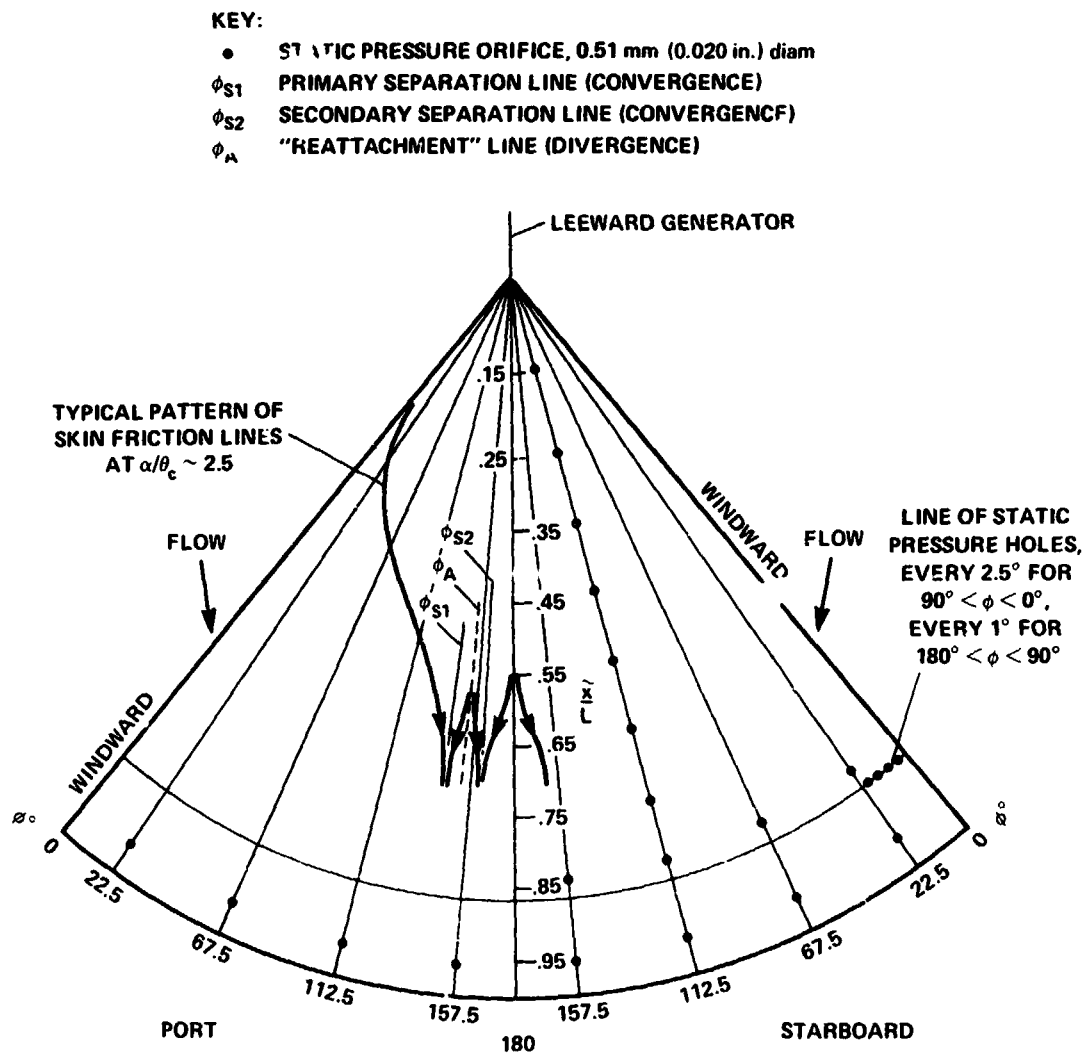
Fig. 10. Unwrapped cone surface.

LASER VAPOR SCREEN,
$\alpha/\theta_c \sim 2.5$, $M_\infty = 0.6$, $R_{L_\infty} = 13.5 \times 10^6$

$\phi = 1 \, 3^\circ$

CONE
SURFACE

CONE BASE

$\phi = 90^\circ$

VIEW LOOKING UPSTREAM FROM CONE BASE,
AT AXIAL STATION, 0.87 L, WHERE $\bar{h}_{CORE} \sim 0.16$

Fig. 11. Laser vapor screen, $\alpha/\theta_c \sim 2.5$, $M_\infty = 0.6$, $R_{L_\infty} = 13.5 \times 10^6$.

VAPOR SCREEN BOUNDARY
(SEE FIG. 11)

$R_{L_\infty} = 13.5 \times 10^6$

4% NOSE BLUNTNESS
AXIAL STATION, 0.87 L

CONTOURS OF CONSTANT
$C_{pp} = (p_p - p_\infty)/q_\infty$

NONDIMENSIONAL HEIGHT ABOVE CONE SURFACE, $\bar{z}$

0.25
0.27
0.29
0.25
0.2
0.1
0.1
0.2 0.3 0.5
0.7 0.6 0.5 0.5

CIRCUMFERENTIAL ANGLE, ϕ deg
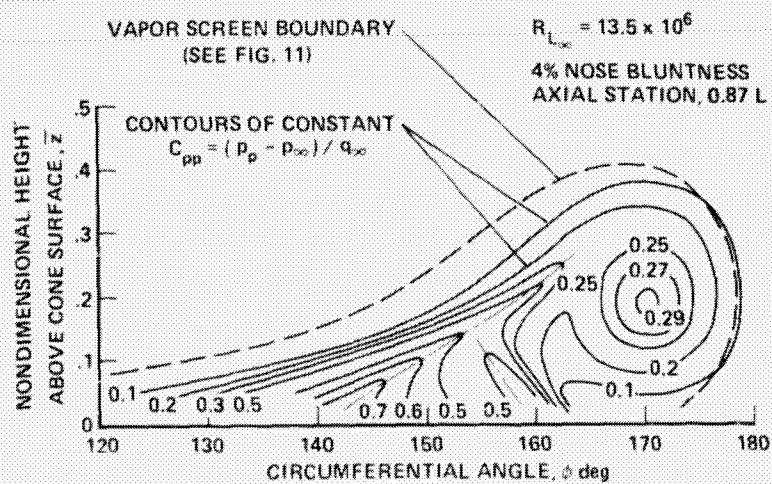
Fig. 12. Pitot pressure deficit, $M_\infty = 0.6$, $\alpha/\theta_c \sim 2.5$.
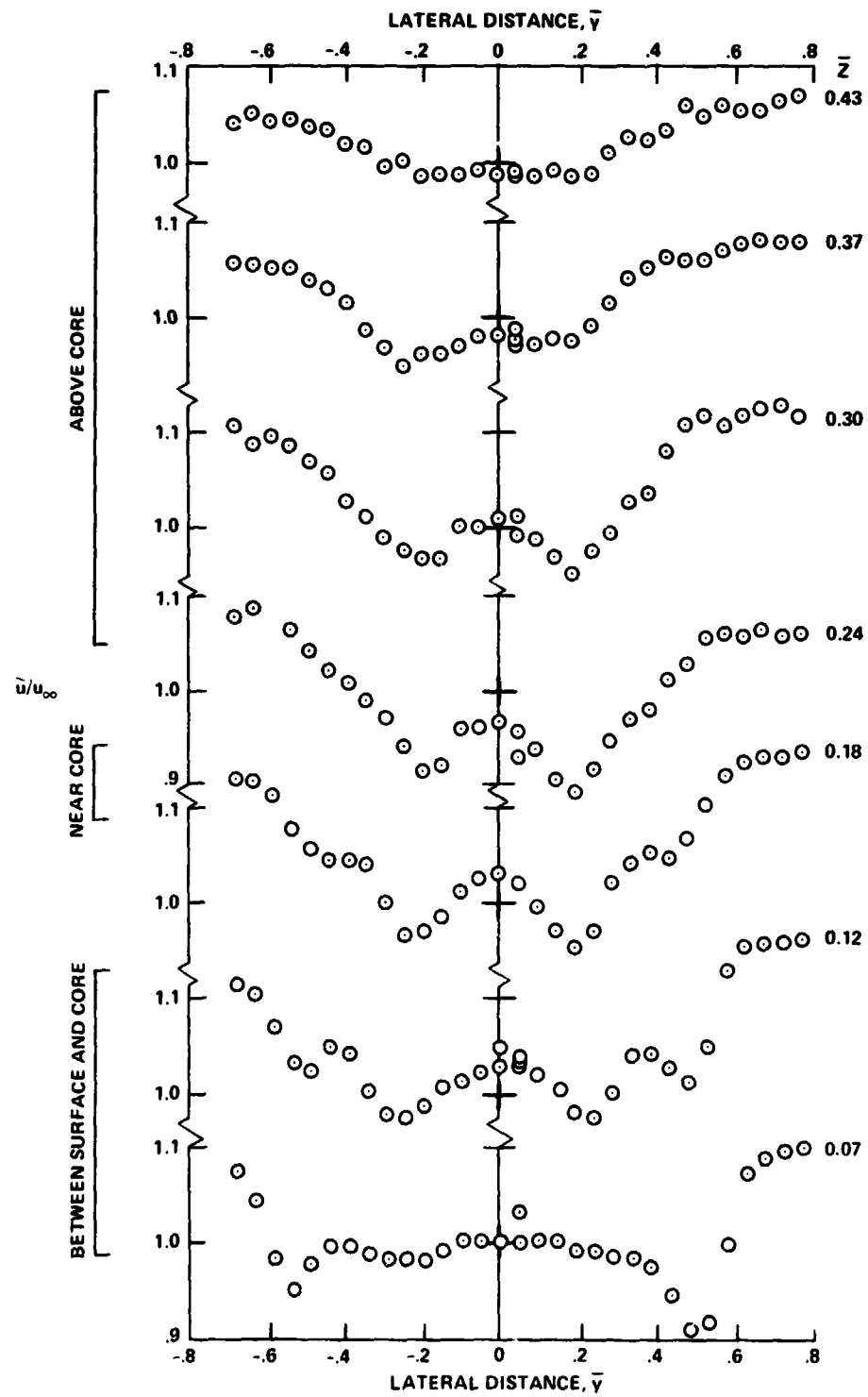
Fig. 13. Mean axial velocities in cross-flow plane at x/L = 0.87, α/θ_c = 2.5.
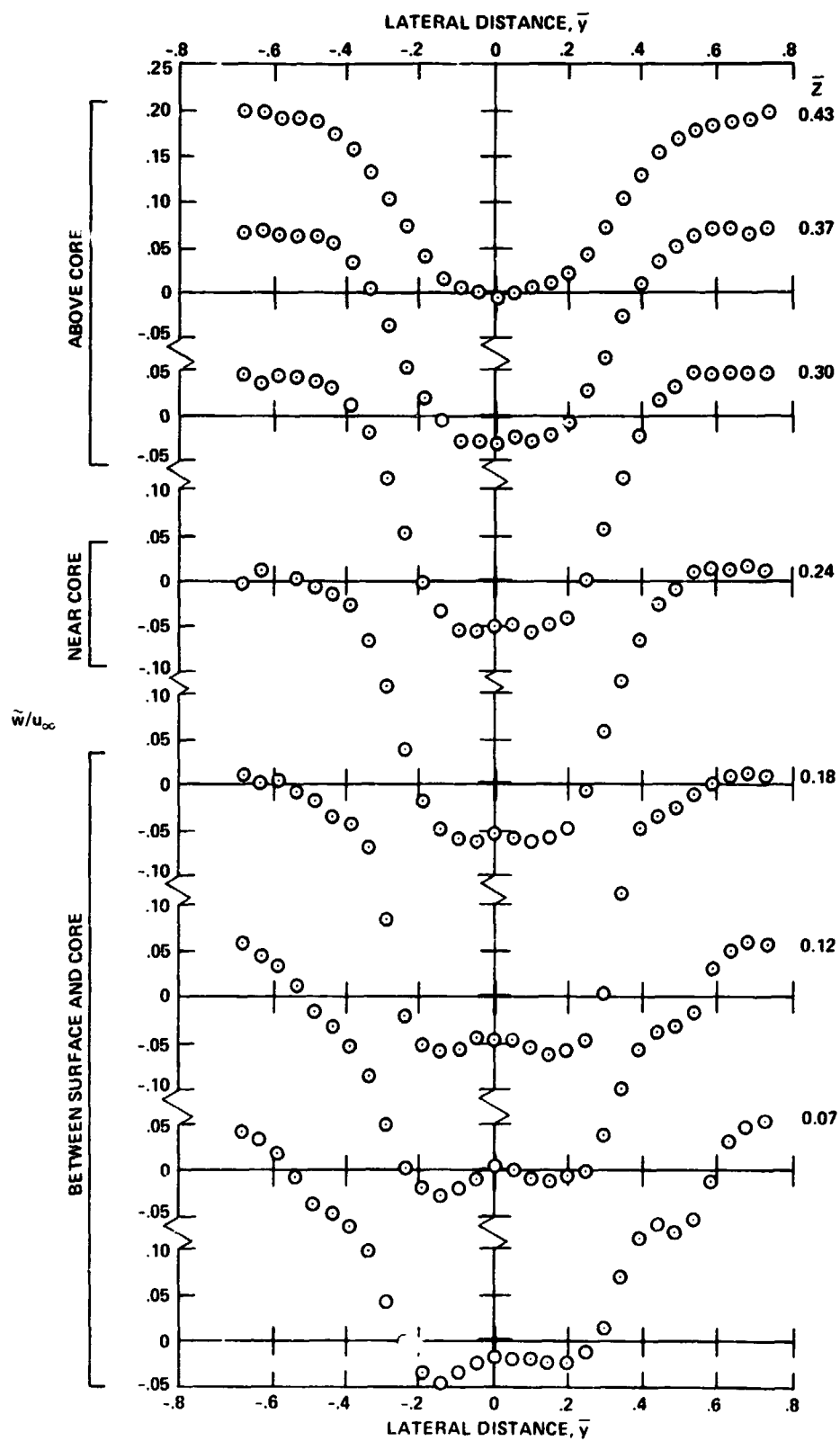
Fig. 14. Mean vertical velocities in cross-flow plane at x/L = 0.87, α/θ$_c$ = 2.5.
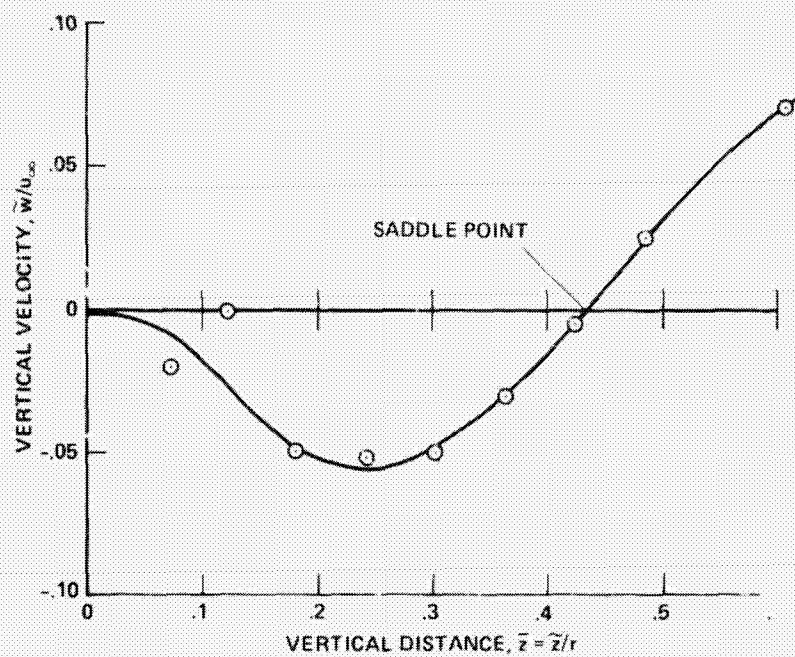
Fig. 15. Vertical velocity in meridian plane,
$\alpha/\theta_c = 2.5$.
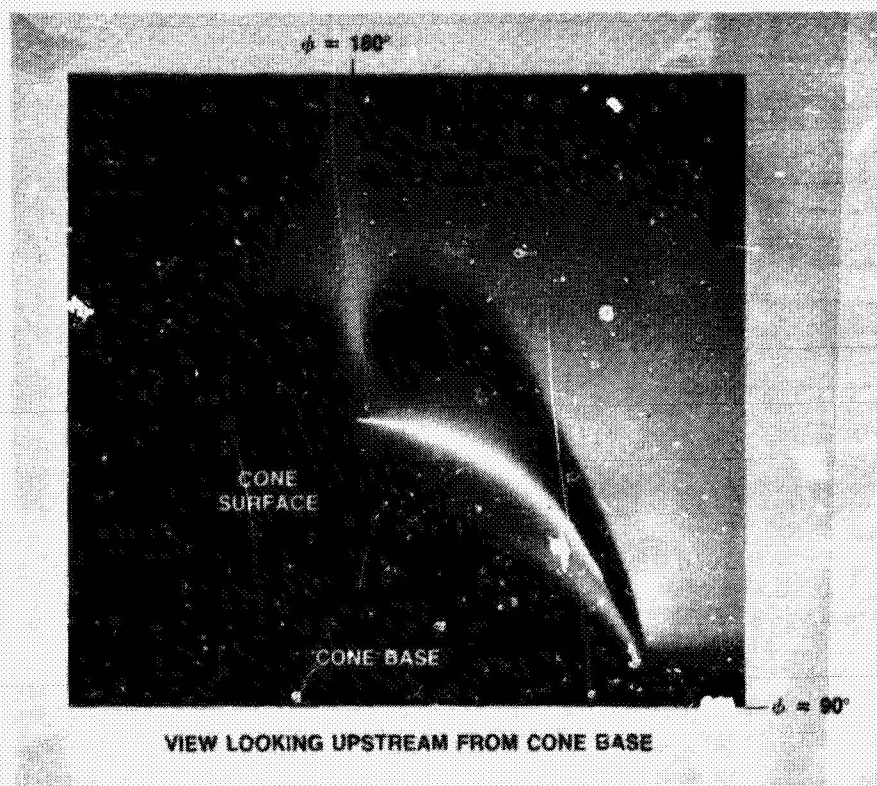
Fig. 16. Laser vapor screen, asymmetry commencing:
$M_\infty = 0.6$, $\alpha/\theta_c = 2.9$.

Fig. 17. Laser vapor screen of asymmetrical vortices
at $\alpha/\theta_c = 3.2$: oblique (pilot) view from port side.
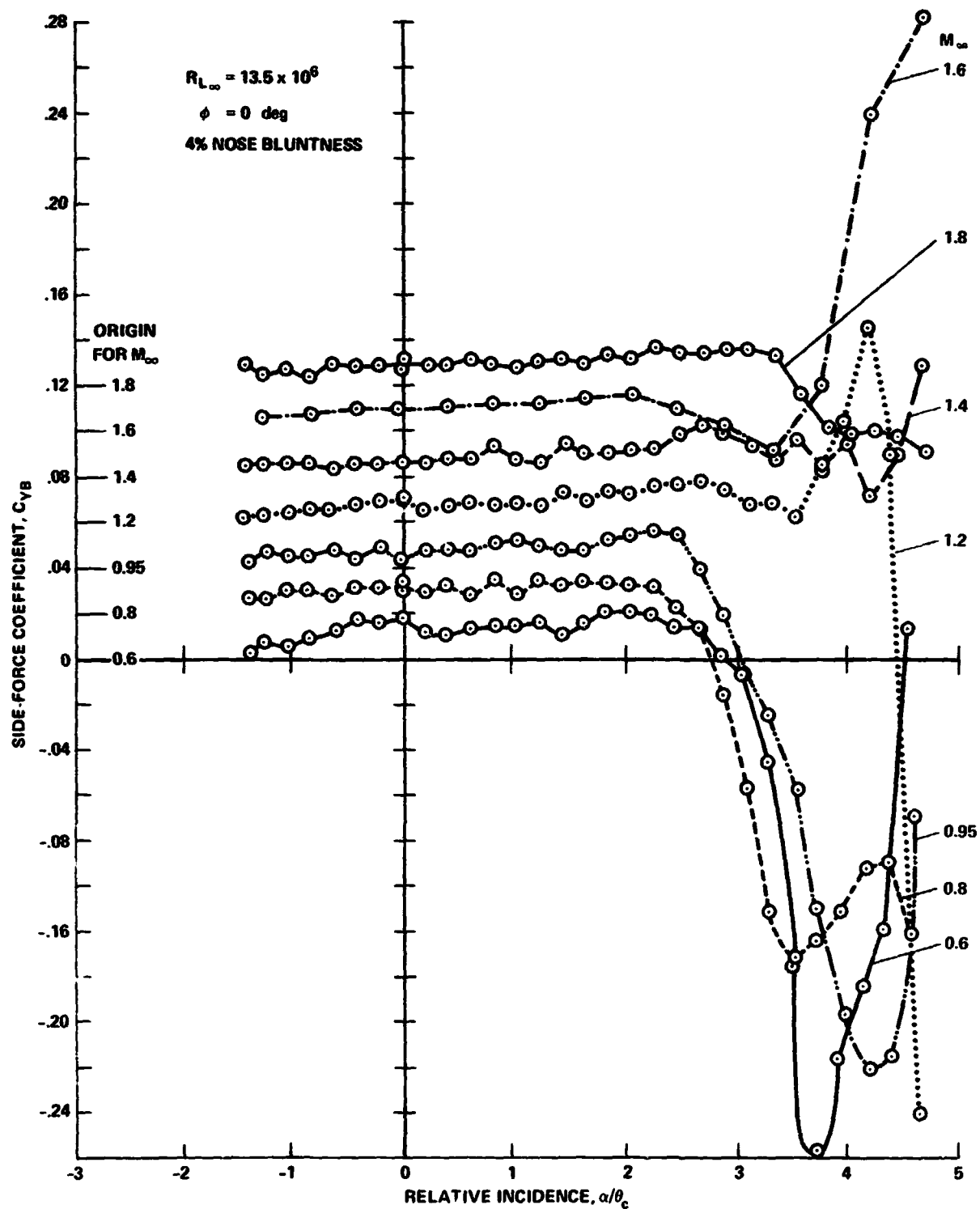
Fig. 18. Side forces on □ ·ted cone, 0.6 < M∞ < 1.8.
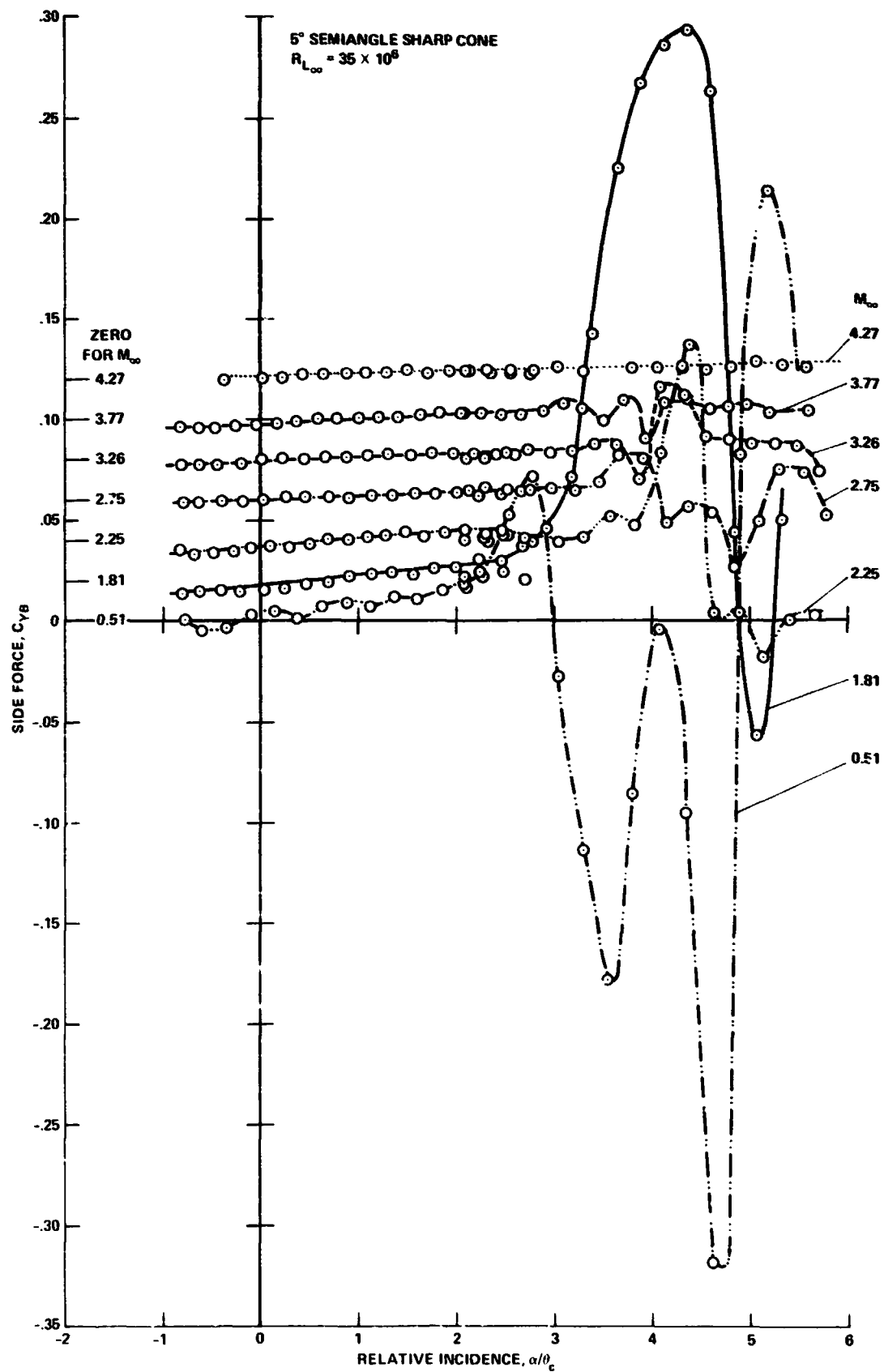
Fig. 19. Side forces on sharp cone, 0.5 < M_∞ < 4.3, at elevated Reynolds number.
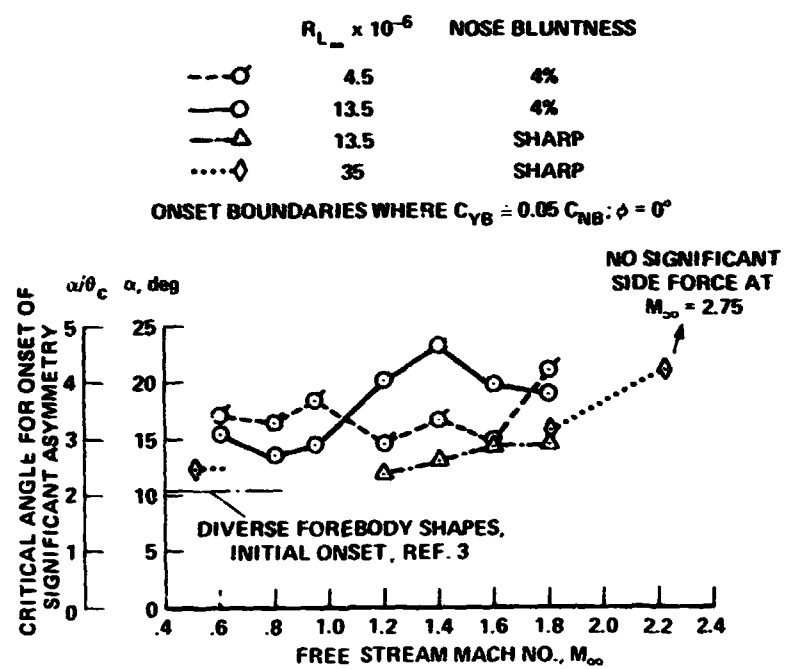
Fig. 20. Onset of significant side-force asymmetry
$(C_{Y\beta} = 0.05\ C_{N\beta})$.
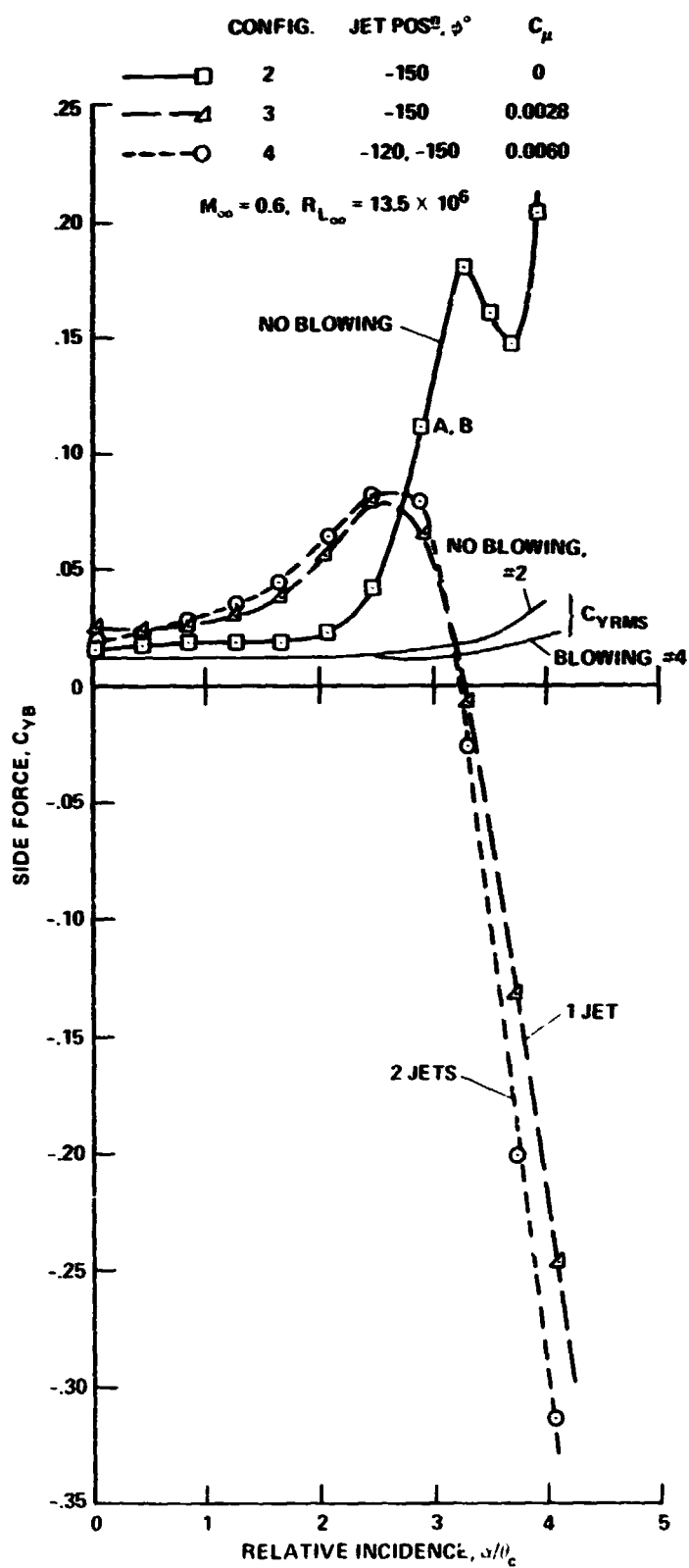
Fig. 21. Incidence/side-force performance with con-
stant normal blowing rate, jet hole
diameter = 2.4 mm (0.096 in.).

	CONFIG.	JET POSⁿ, φ°	C_μ
▽	5	150	0
△△	6	150	0.006
◁	7	0, 150	PASSIVE
◻	8	0, ±150	0.0098

$M_\infty = 0.6$, $R_{L_\infty} = 13.5 \times 10^6$

ASYMMETRIC

NO BLOWING

SYMMETRIC

PASSIVE

SIDE FORCE, C_{YB}

RELATIVE INCIDENCE, α/θ_c
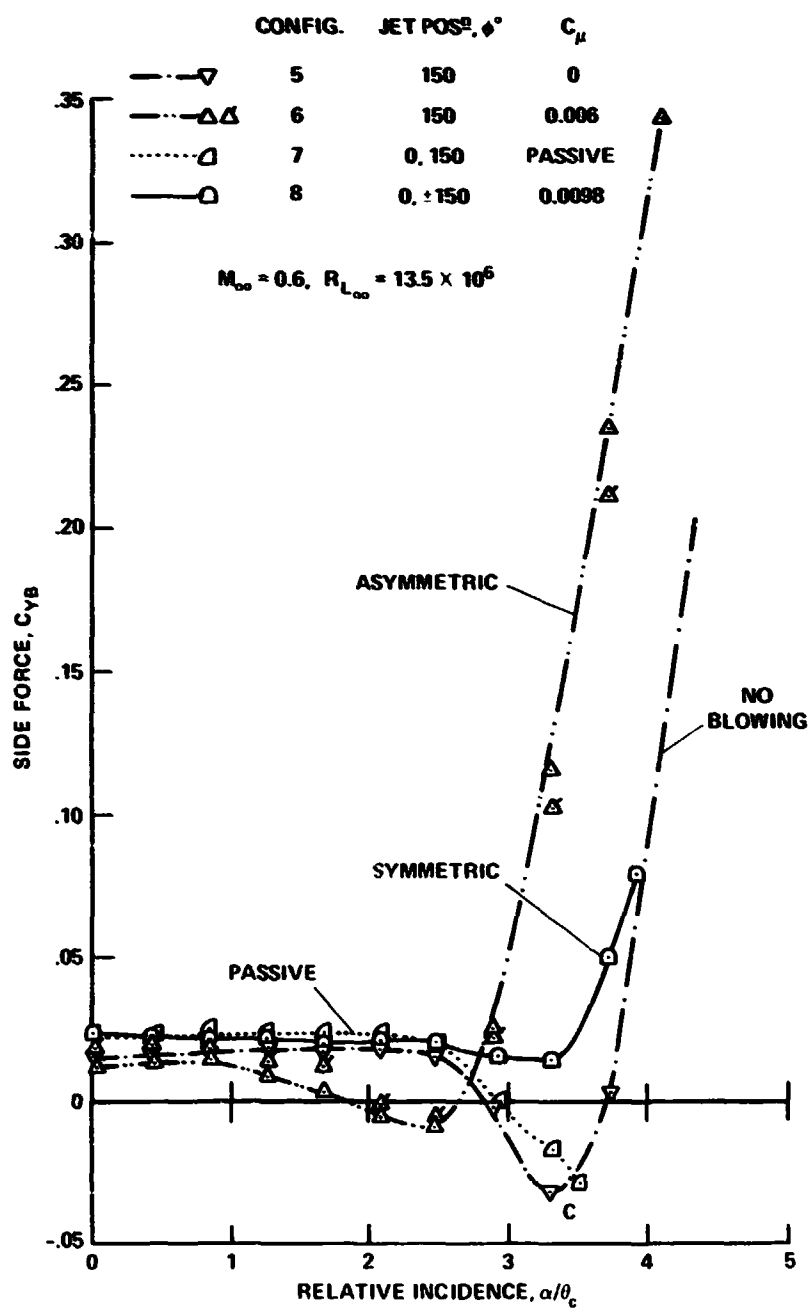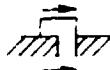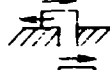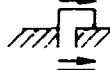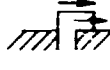
Fig. 22. Incidence/side-force performance with constant normal blowing rate, jet hole diameter = 3.6 mm (0.140 in.).

	CONFIG.	JET POS$^{\underline{N}}$, ϕ°	BLOWING	c_μ	JET diam, mm (in.)
—————◊	9	150		0	3.4 (0.132)
– – – –△	10	150		0.0054	3.4 (0.132)
— — —◊	11	150		0	3.4 (0.132)
·········O	12	150		0.0056	3.4 (0 132)

BLOWING
UPSTREAM

BLOWING
DOWNSTREAM

NO BLOWING

SIDE FORCE, C_{YB}

RELATIVE INCIDENCE, α/θ_c
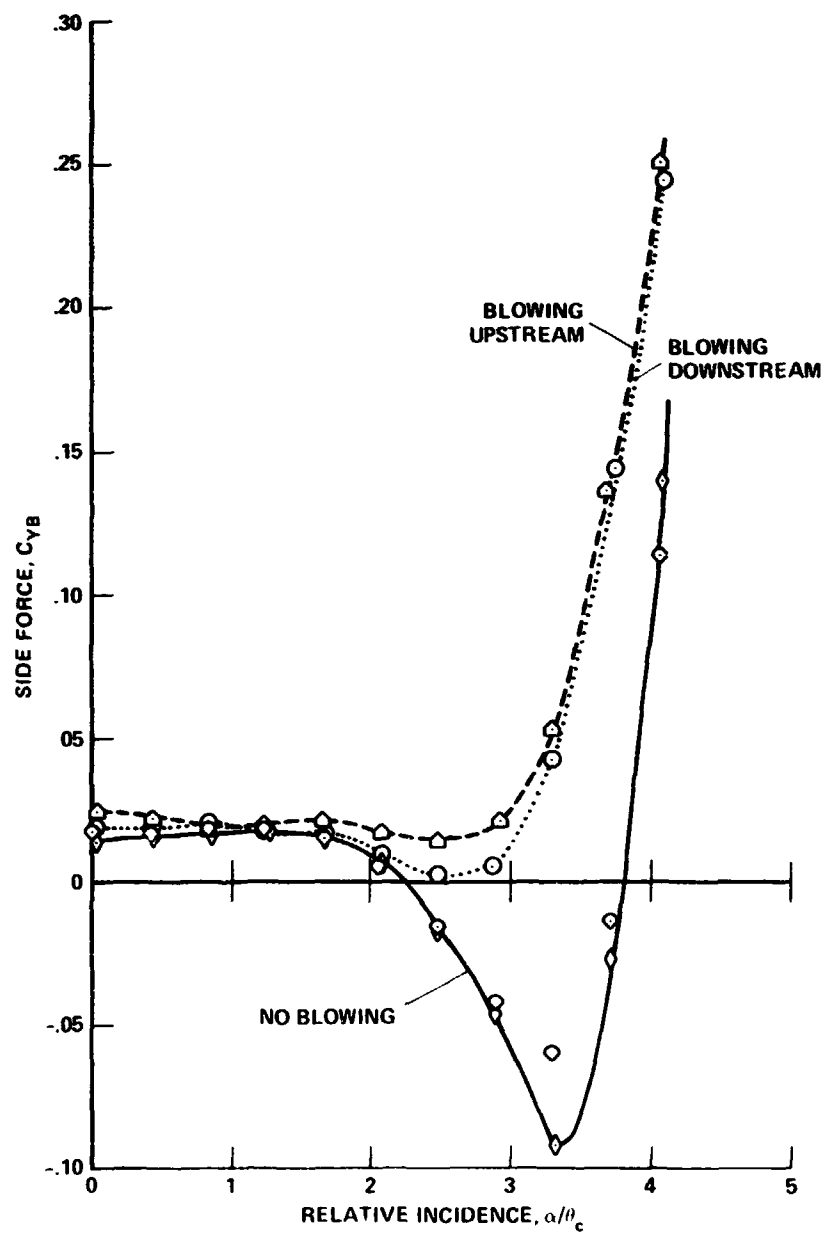
Fig. 23.   Incidence/side-force performance with con-
stant tangential blowing rate, jet hole
diameter = 3.4 mm (0.132 in.).
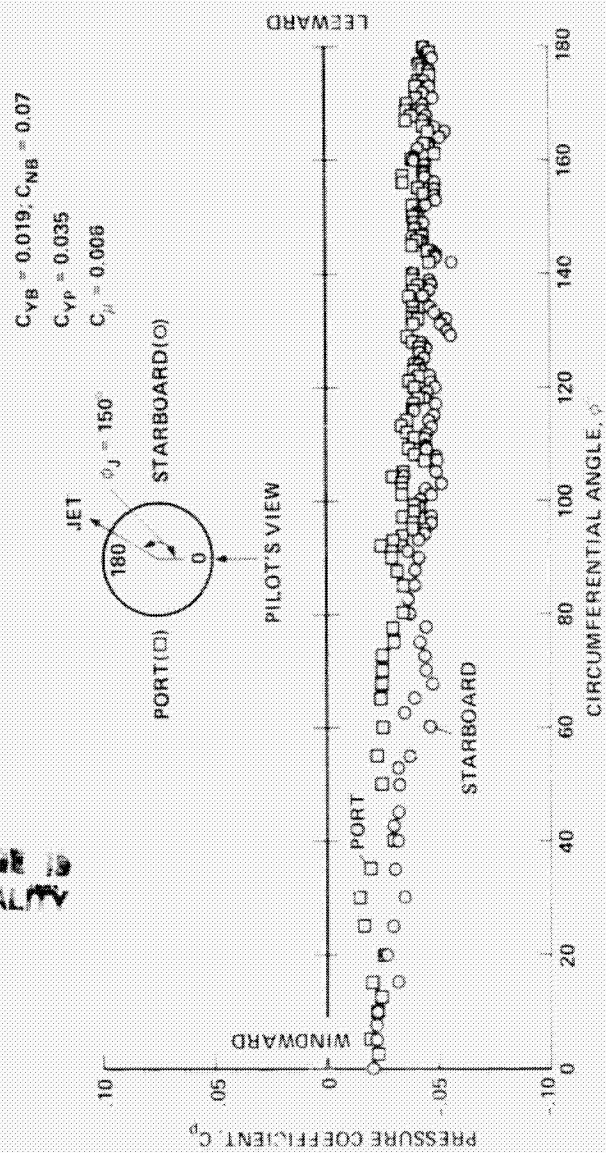
(a) $\alpha/\theta_c = 0.44$.

Fig. 24. Effect of changing incidence at constant blowing rate, $C_\mu = 0.006$: laser vapor screen and circumferential pressures at x/c = 0.87 (Configuration 6).
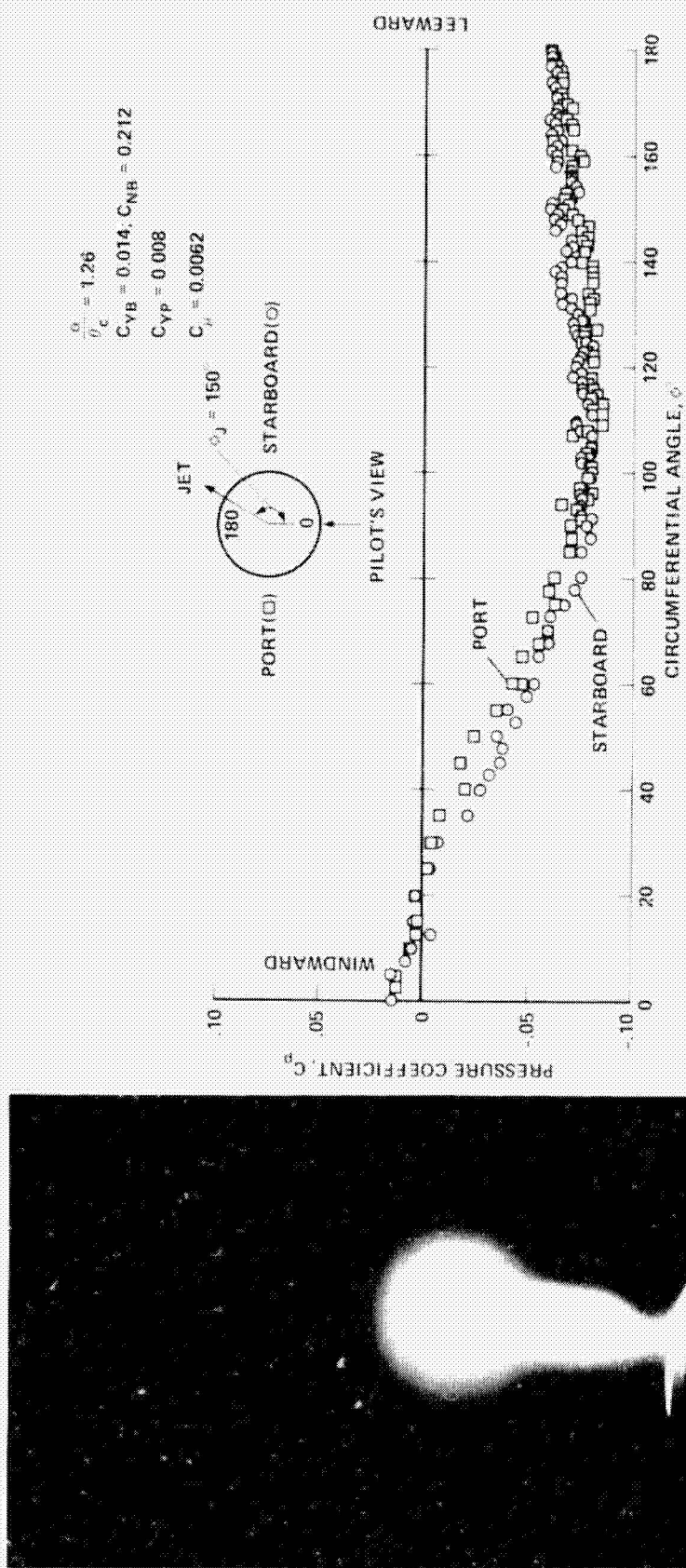
(b) $\alpha/\theta_C = 1.26$.

Fig. 24. Continued.
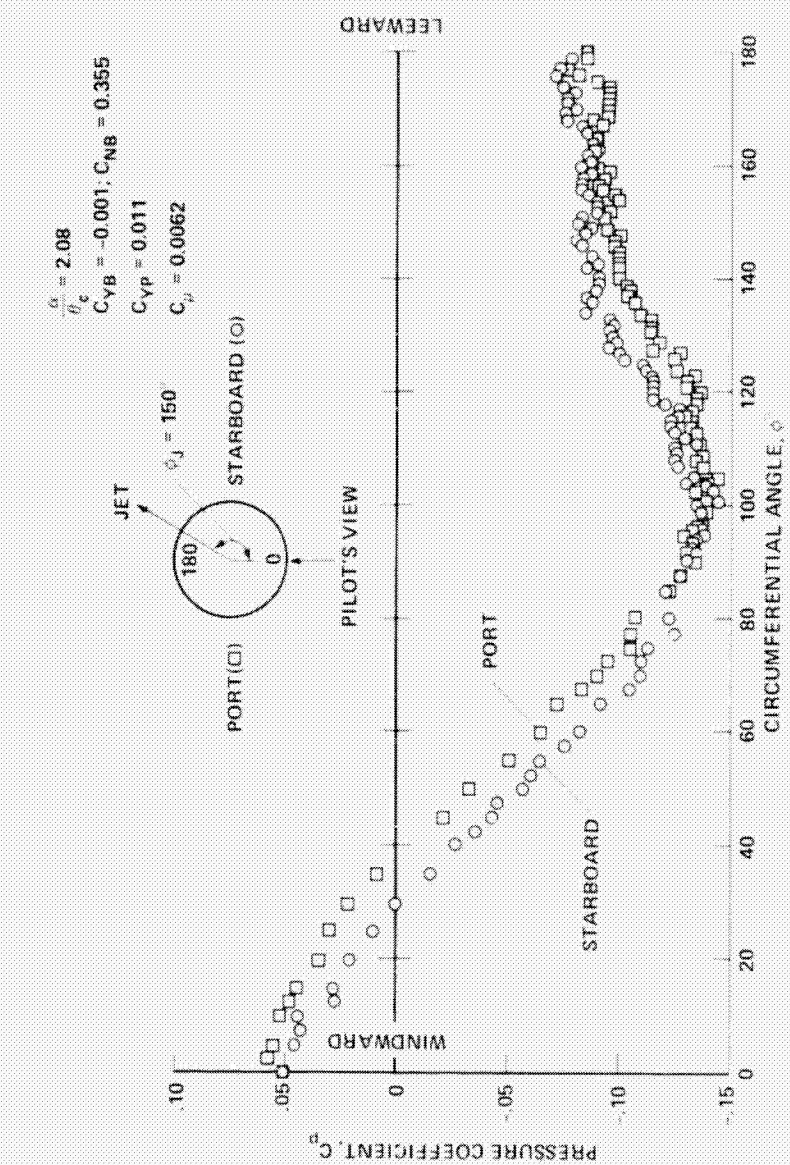
(c) $\alpha/\theta_C = 2.08$.

Fig. 24. Continued.

CHANGING INCIDENCE AT FIXED BLOWING.
$C_\mu = 0.006$

$\dfrac{\alpha}{\theta_c} = 2.48$

$C_{YB} = -0.006; C_{NB} = 0.432$

$C_{YP} = 0.026$

$C_\mu = 0.0062$

JET $\phi_J = 150$

PORT(□)   STARBOARD(○)

PILOT'S VIEW

LEEWARD

PORT

STARBOARD

WINDWARD

PRESSURE COEFFICIENT, C_p

CIRCUMFERENTIAL ANGLE, ϕ
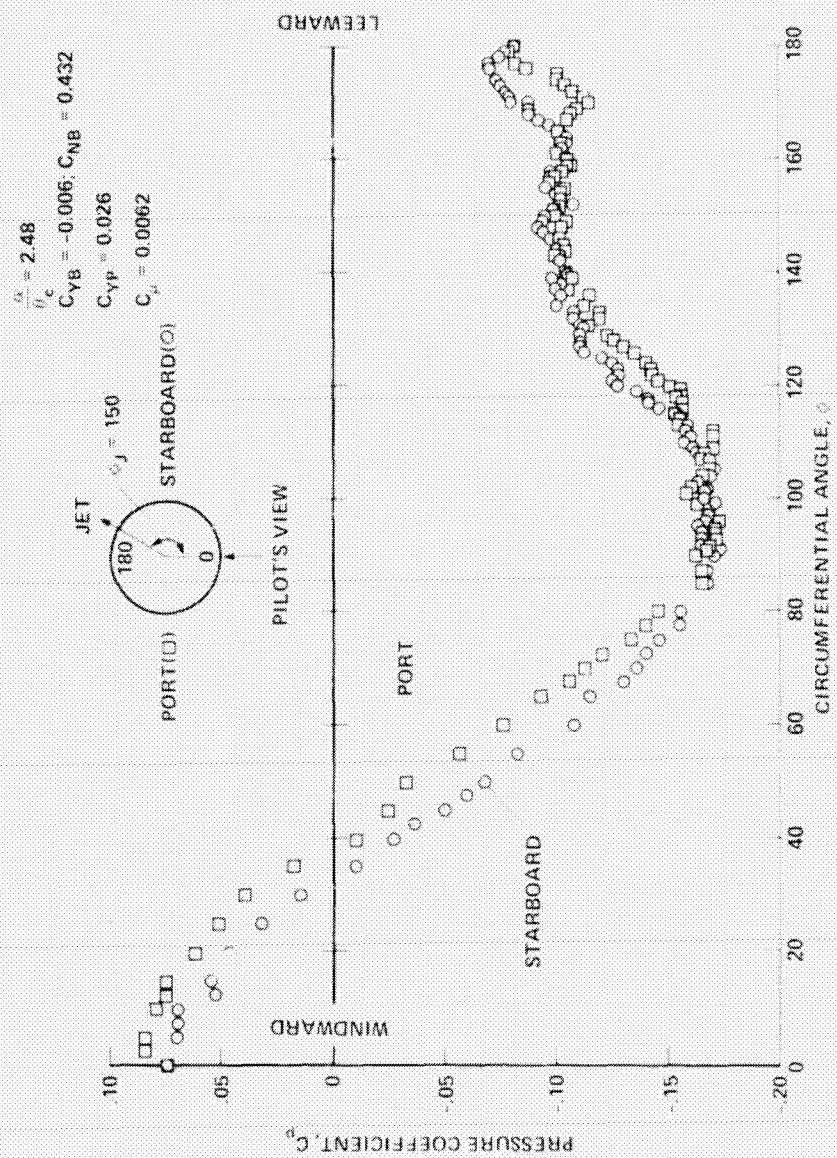
(d) $\alpha/\theta_c = 2.48$.
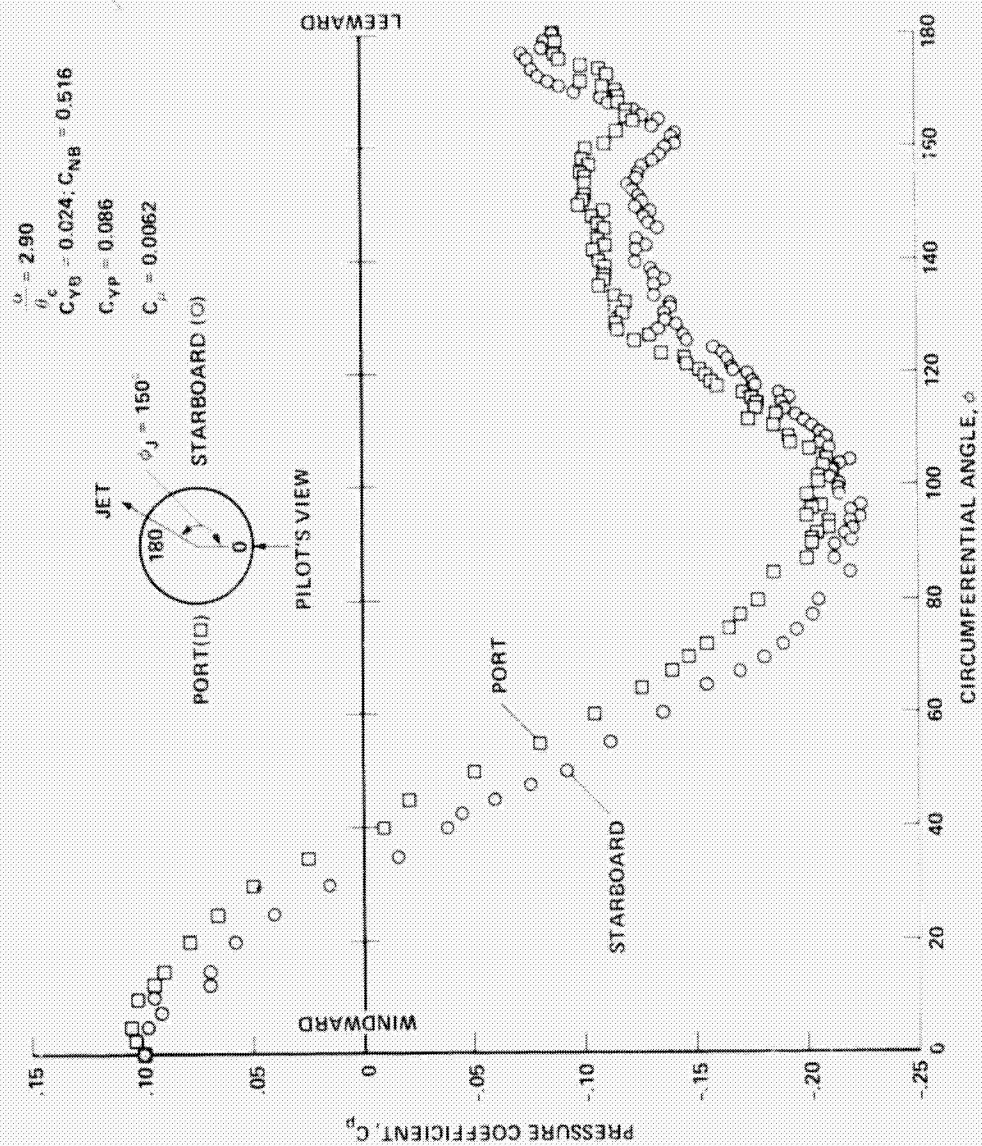
Fig. 24. Continued.

(e) $\alpha/\theta_c = 2.9$.

Fig. 24. Continued.

(f) $\alpha/\theta_c = 3.7$.

Fig. 24. Concluded.

Σ_N = NO. OF FOCI $\circlearrowleft$ = 6

Σ_S = NO. OF SADDLE POINTS = 3

$\Sigma_{S'}$ = NO. OF HALF SADDLES ON SURFACE = 8

$\therefore \Sigma_N - (\Sigma_S + \frac{1}{2}\Sigma_{S'}) = -1$

THIS SATISFIES CROSS-FLOW TOPOLOGY LAW, REFS. 21, 22

JET VORTICES

FOREBODY PRIMARY VORTICES

FOREBODY SECONDARY VORTICES

7 "HALF-SADDLE" POINTS

S', HALF-SADDLE ON WINDWARD ATTACHMENT LINE IS OUT OF VIEW
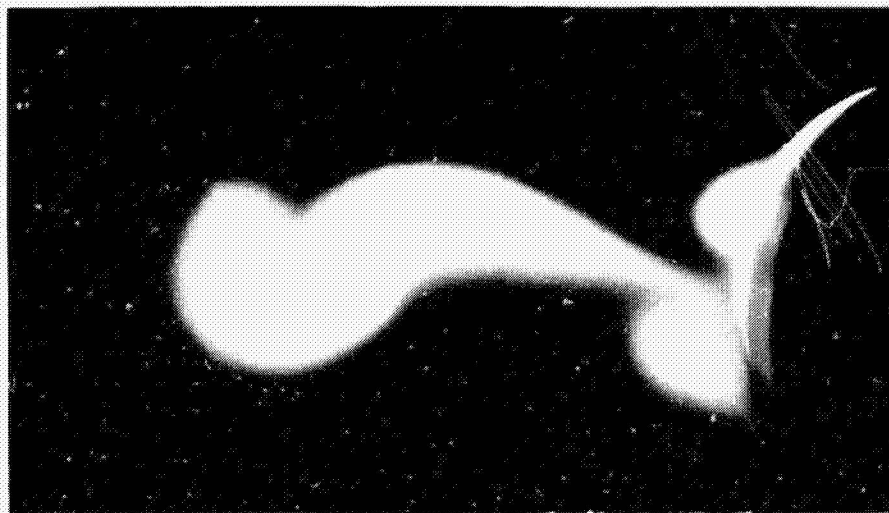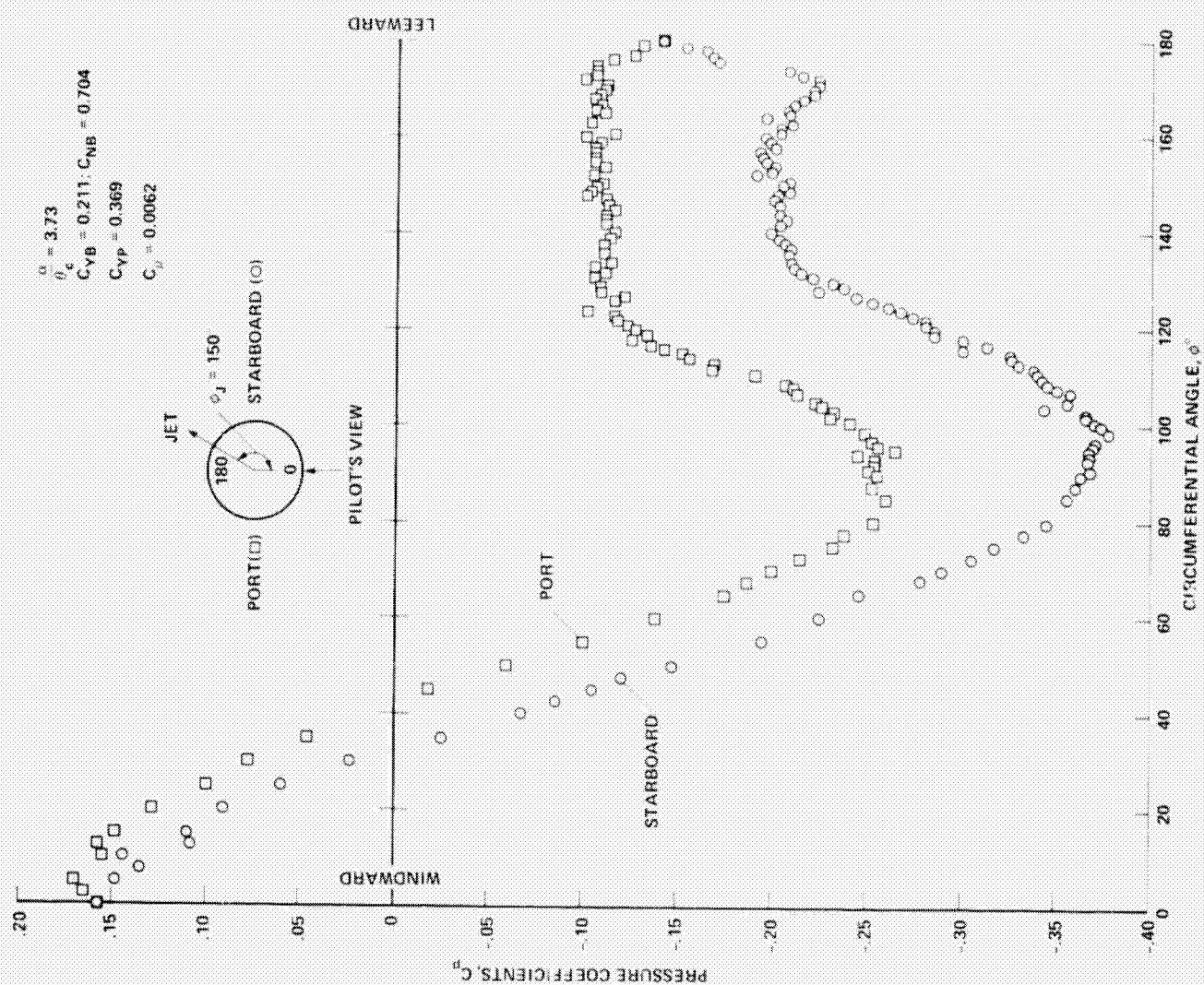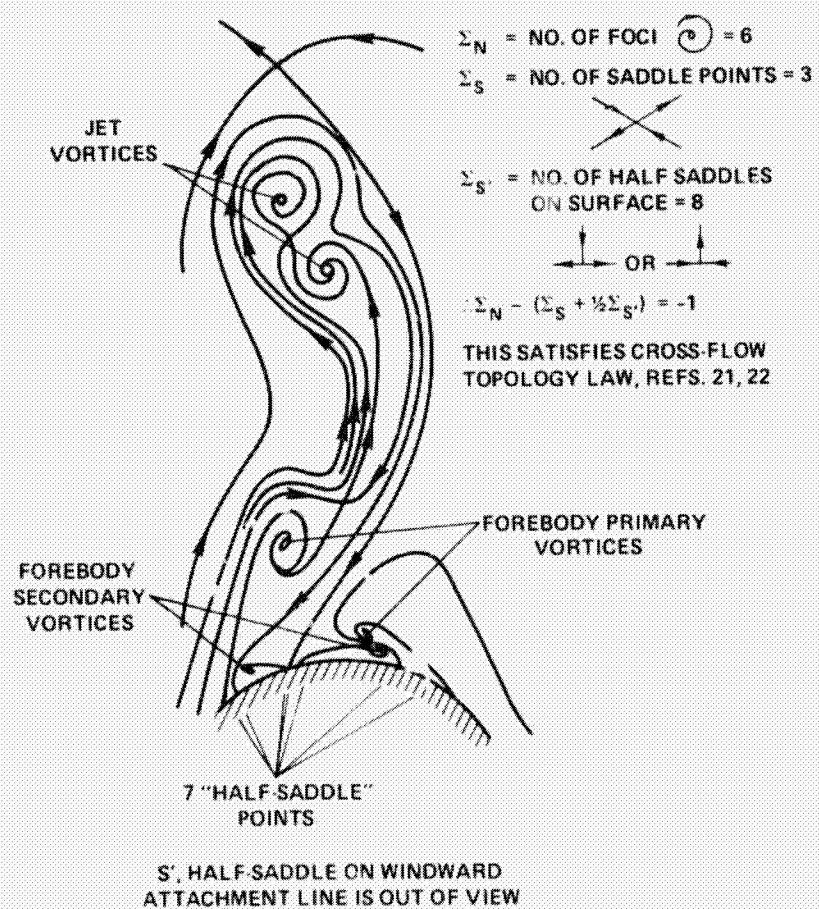
(a) Close-coupled jet vortices and "high" forebody vortices.

Fig. 25. Hypothesized flow structures of jet and forebody vortices.

Σ_N = NO. OF FOCI $\circlearrowleft$ = 6

Σ_S = NO. OF SADDLES = 3

$\Sigma_{S'}$ = NO. OF HALF SADDLES ON SURFACE = 8

$\Sigma_N - (\Sigma_S + \tfrac{1}{2}\Sigma_{S'}) = -1$

THIS SATISFIES CROSS-FLOW TOPOLOGY LAW, REFS. 21, 22

JET VORTICES

FOREBODY SECONDARY VORTICES

FOREBODY PRIMARY VORTICES

7 "HALF-SADDLE" POINTS

HALF SADDLE ON WINDWARD ATTACHMENT LINE IS OUT OF VIEW
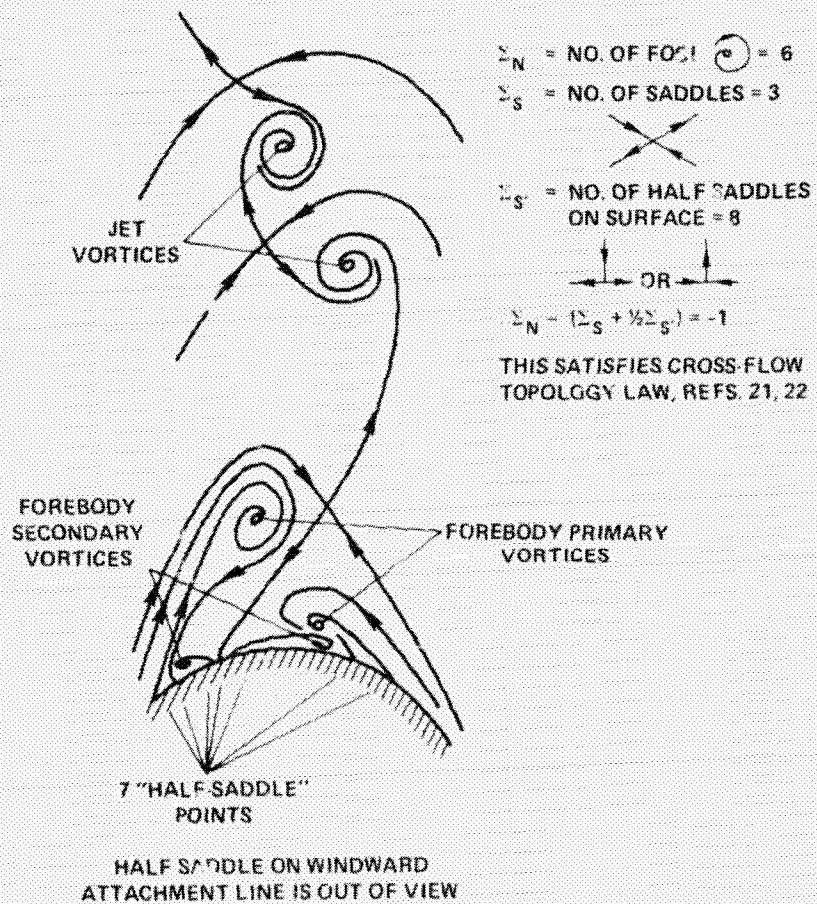
(b) "Separate" jet and forebody vortices.

Fig. 25. Concluded.

15-41
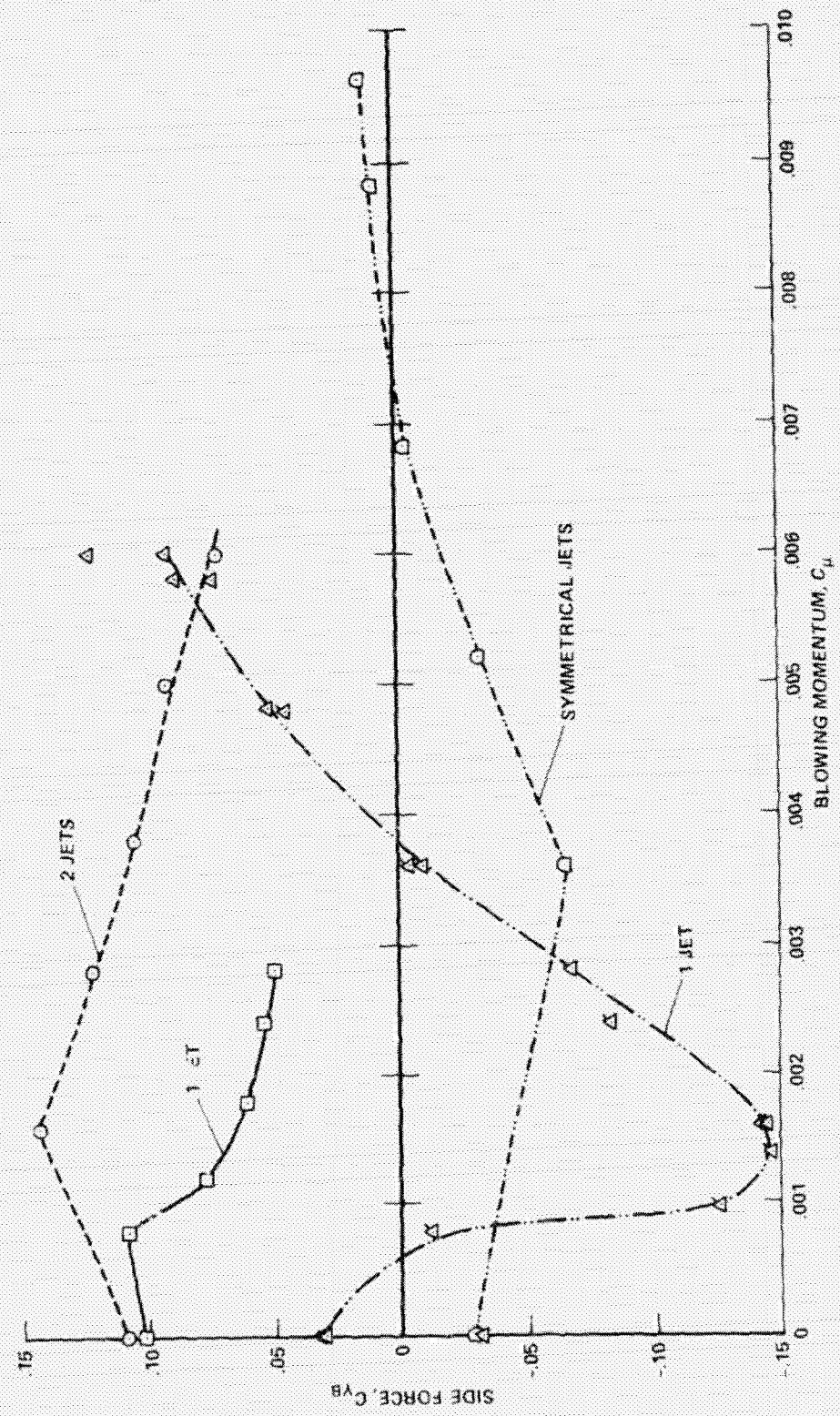
Fig. 26. Effect of normal blowing on side force at constant incidence, $\alpha/\theta_c \sim 3.2$.
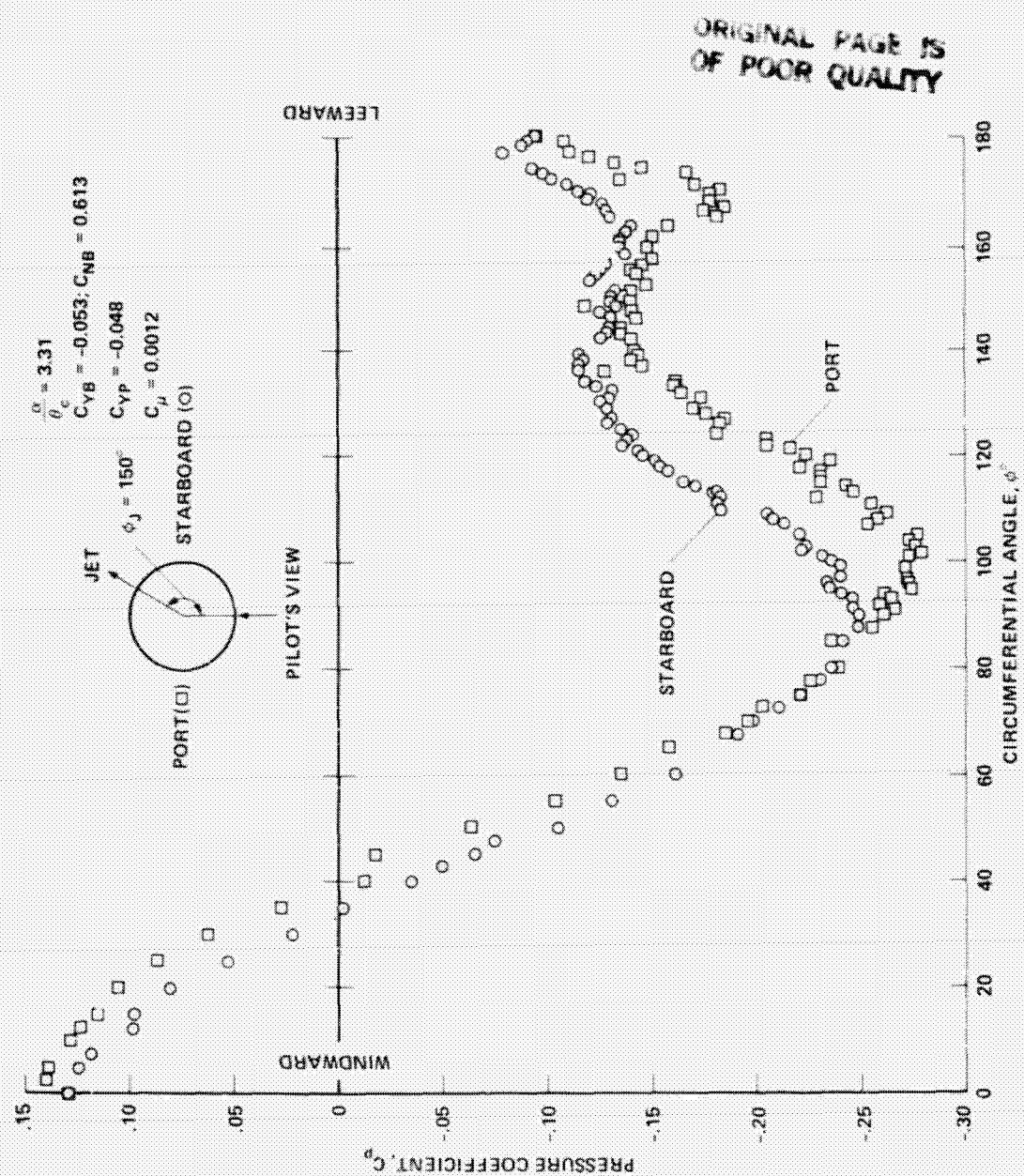
(a) $C_\mu = 0.0012$.

Fig. 27. Changing blowing rate at $\alpha/\theta_c = 3.3$: laser vapor screen and surface pressures at x/L = 0.87 (Configuration 6).
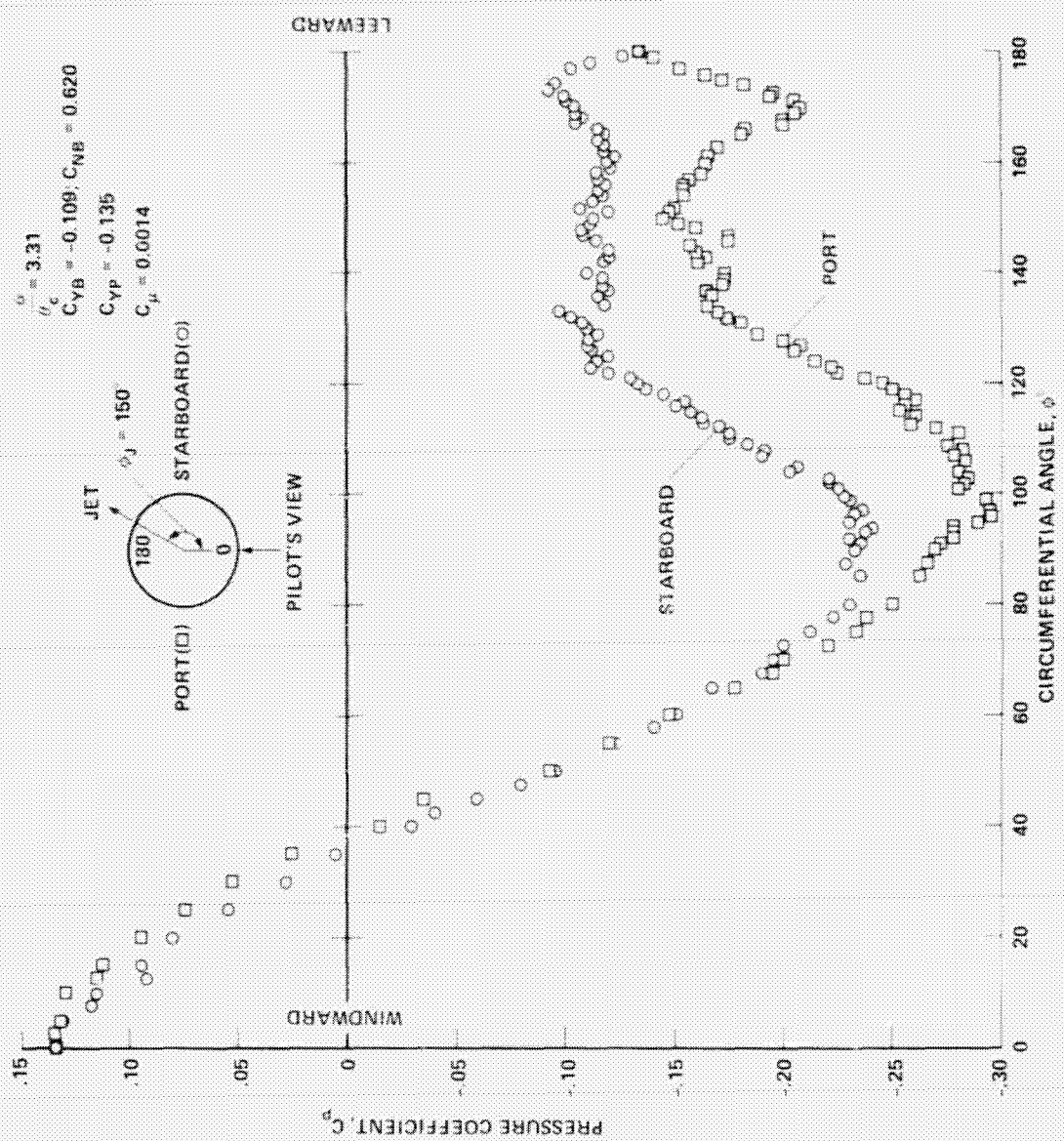
(b) C_μ = 0.0014.

Fig. 27. Continued.
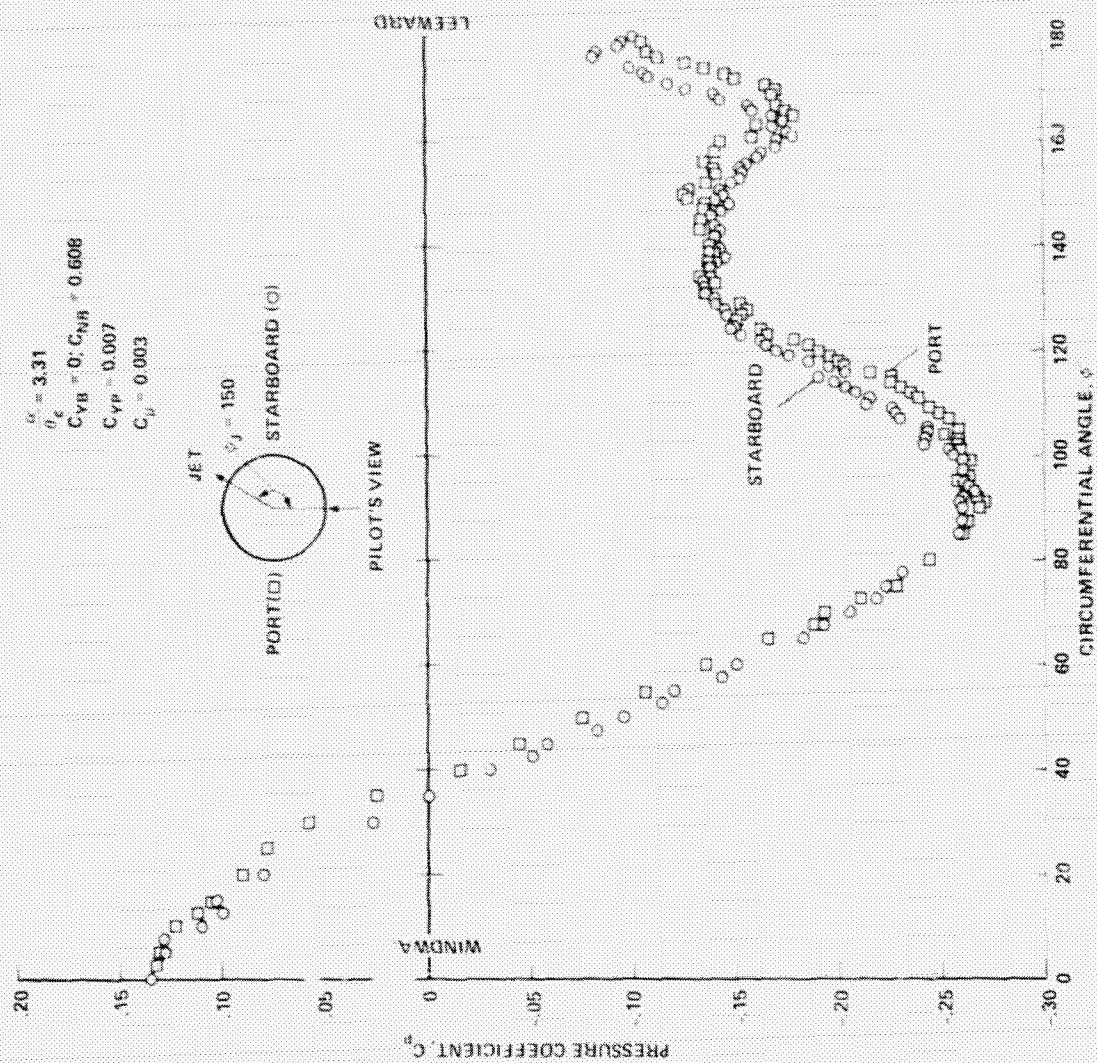
(d) $c_\mu = 0.003$.

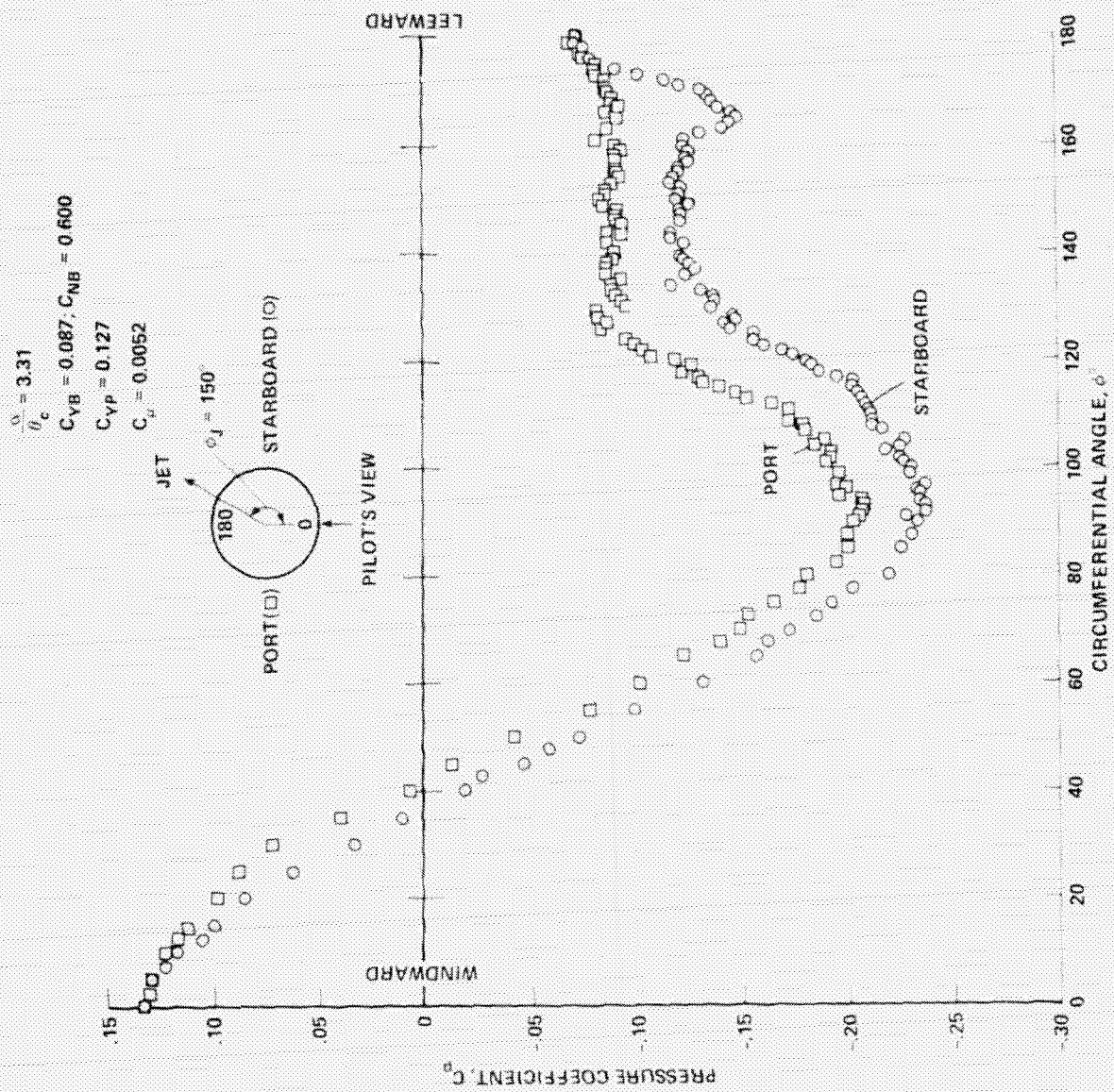Fig. 27. Continued.
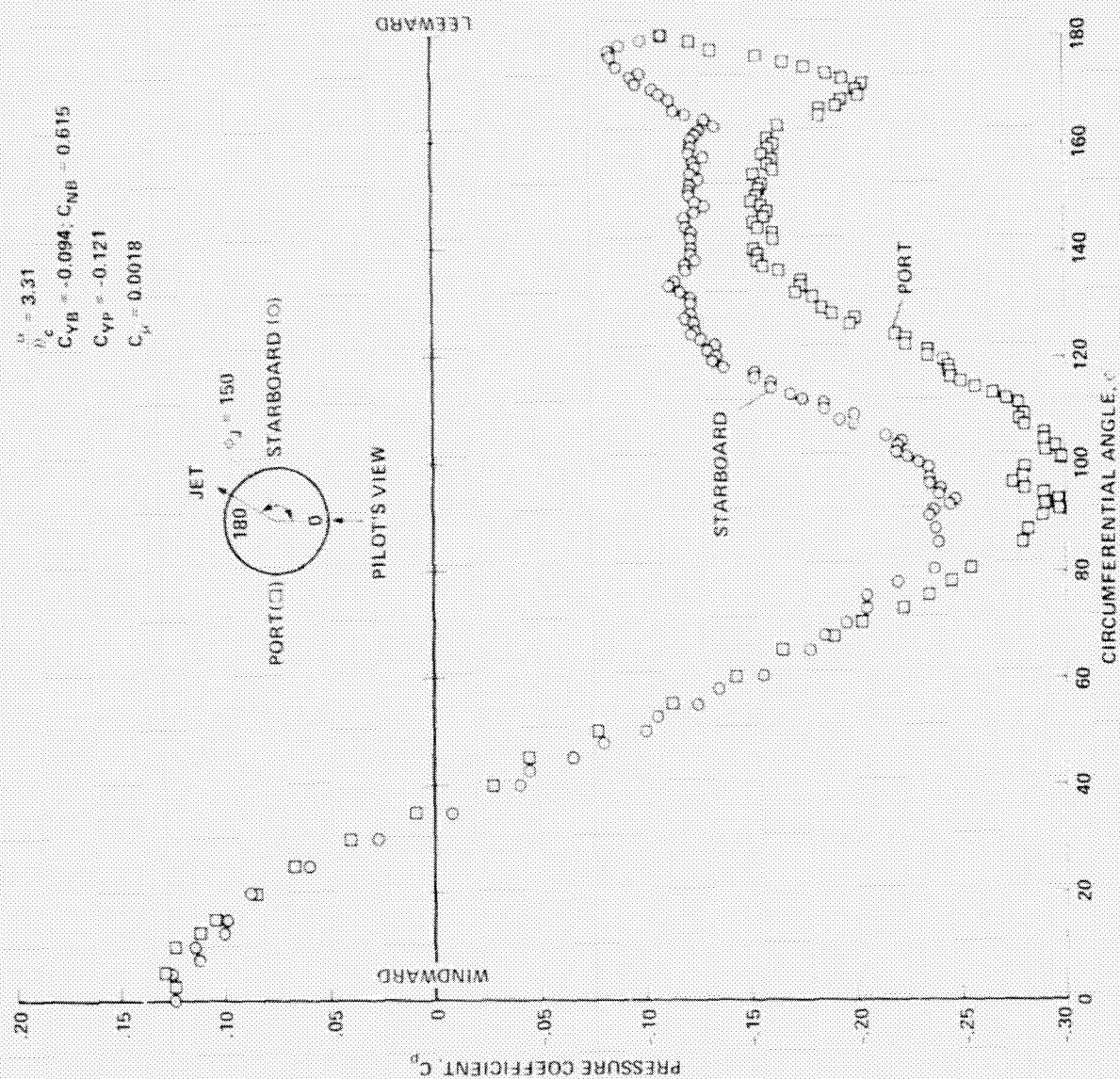
(c) $C_\mu = 0.0018$.
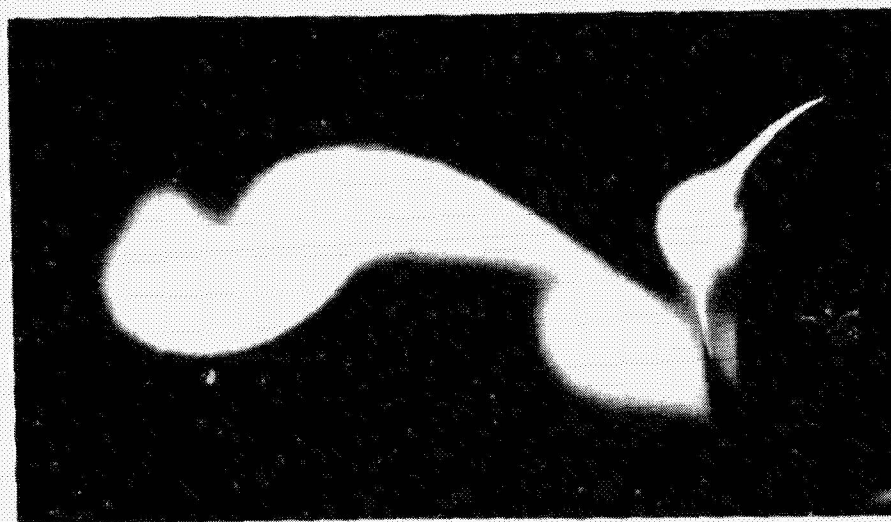
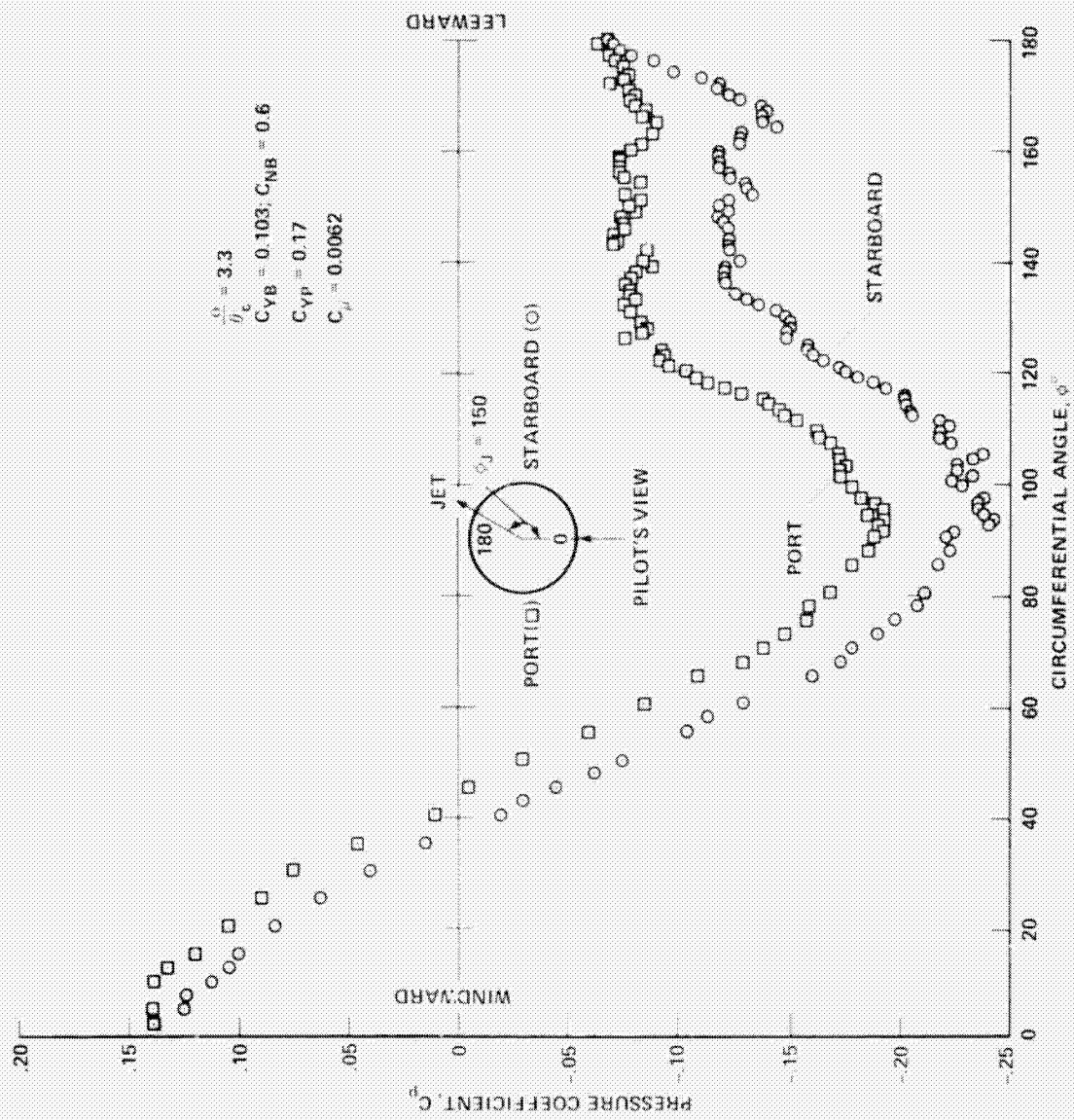Fig. 27. Continued.
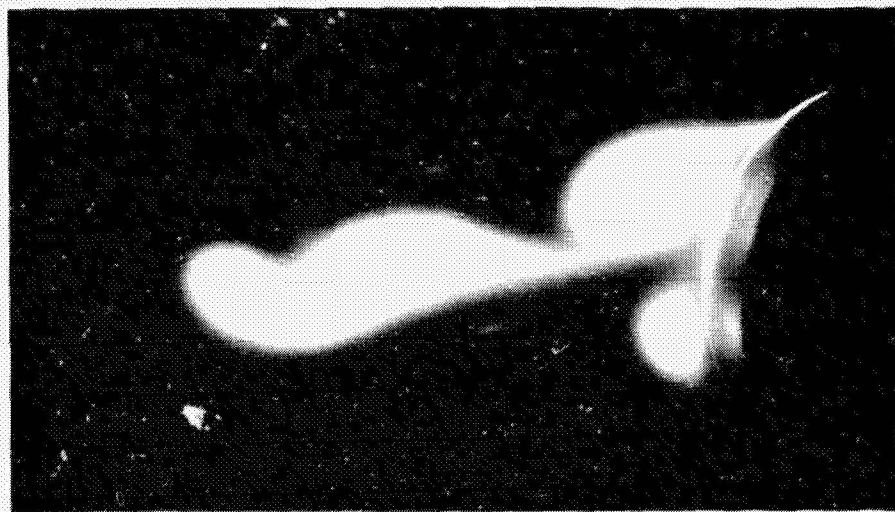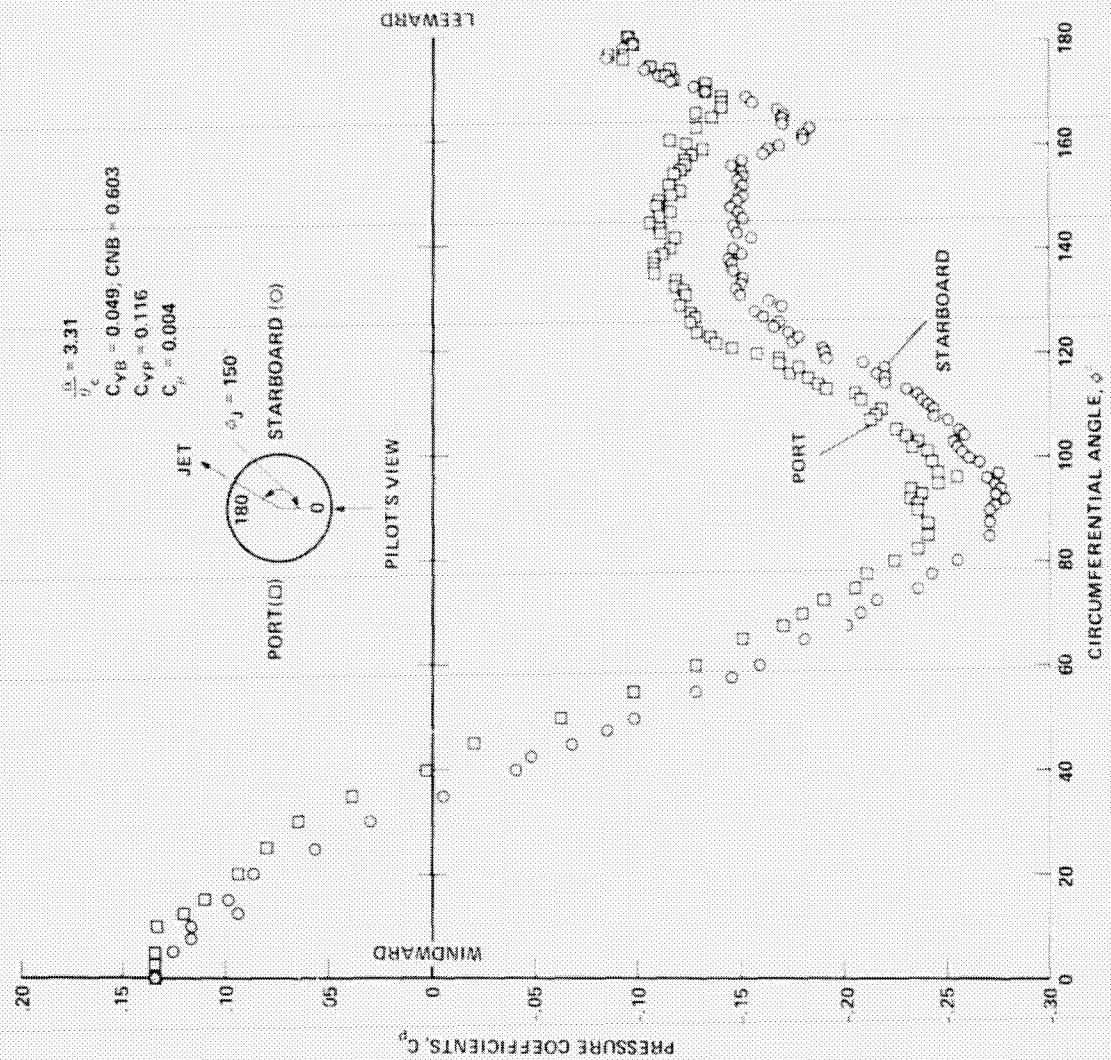
(e) $C_\mu = 0.004$.

Fig. 27. Continued.
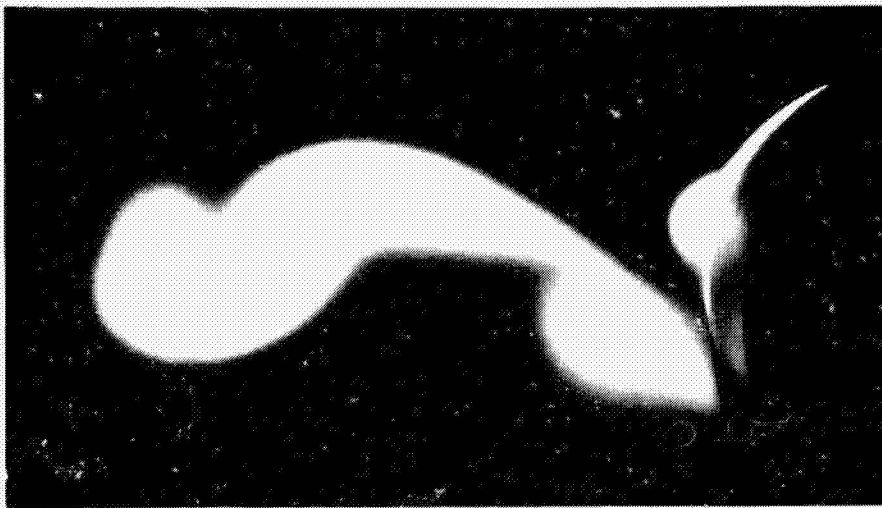
(f) C_μ = 0.0052.
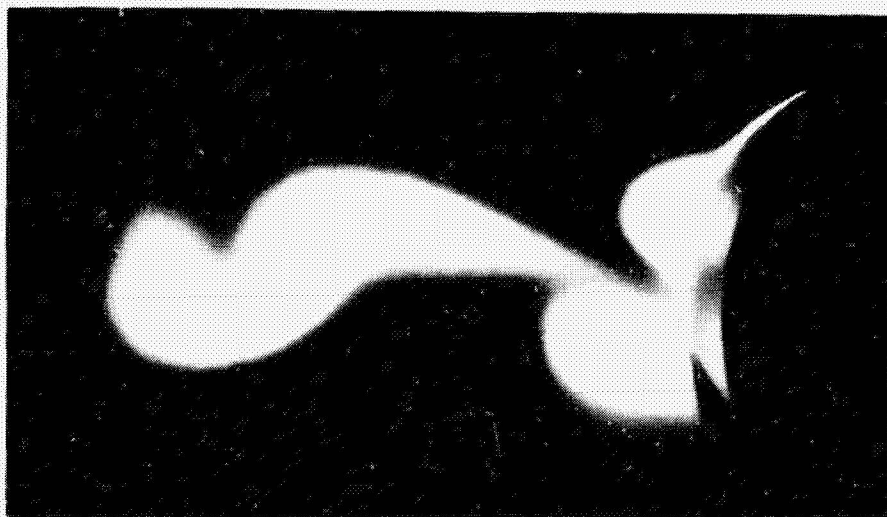
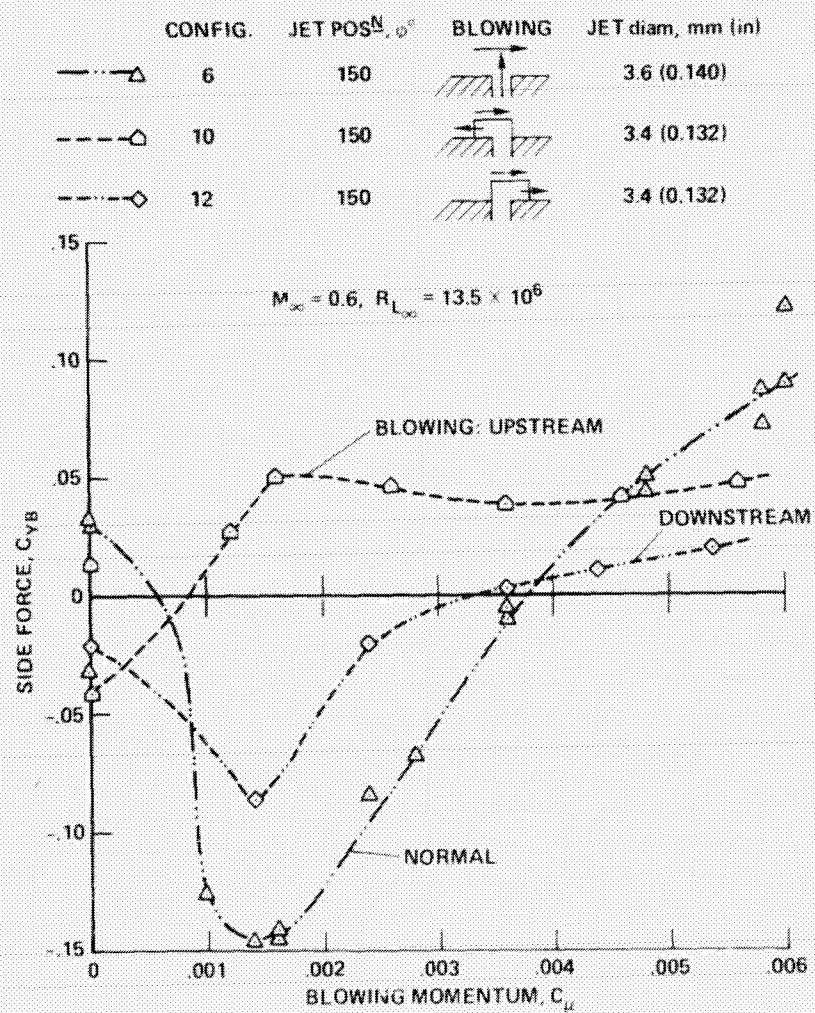Fig. 27. Continued.

(g) $C_\mu = 0.0062$.

Fig. 27. Concluded.

Fig. 28. Reversal of side force: normal and tangential blowing at $\alpha/\theta_c \approx 3.2$.